ELSEVIER

materialstoday

www.materialstoday.com

SEPTEMBER 2021 | VOLUME 48

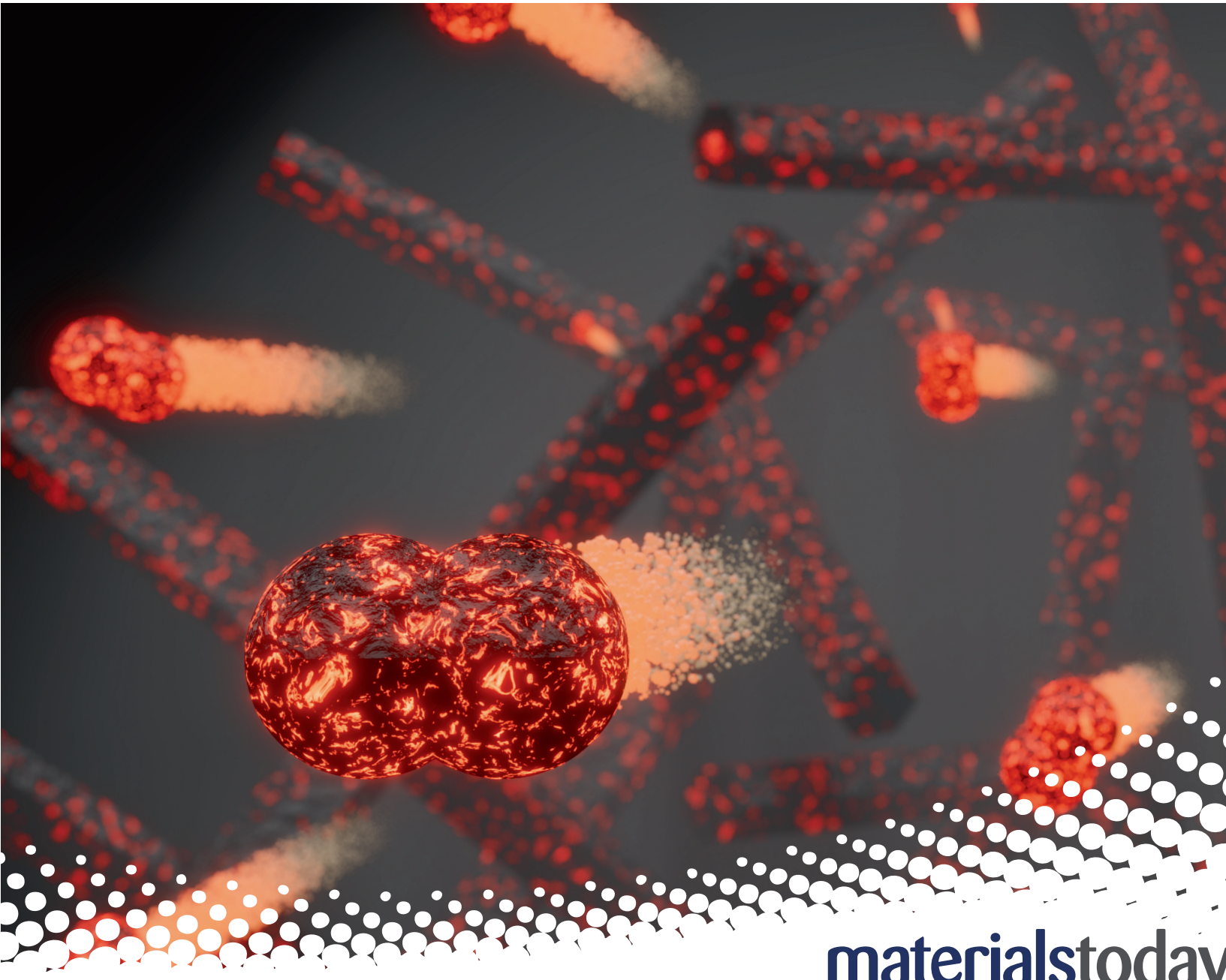

materialstoday
Connecting the materials community

ELSEVIER

Electrically powered repeatable air explosions using microtubular graphene assemblies

Fabian Schütt [1,†,*], Florian Rasch [1,†], Nipon Deka [1], Armin Reimers [1], Lena M. Saure [1], Sören Kaps [1], Jannik Rank [1], Jürgen Carstensen [1], Yogendra Kumar Mishra [2], Diego Misseroni [4], Adrian Romani Vázquez [3], Martin R. Lohe [3,5], Ali Shaygan Nia [3], Nicola M. Pugno [4,6], Xinliang Feng [3], Rainer Adelung [1,*]

[1] Functional Nanomaterials, Institute for Materials Science, Kiel University, Kaiser Str. 2, 24143 Kiel, Germany
[2] Mads Clausen Institute, NanoSYD, University of Southern Denmark, Alsion 2, 6400 Sønderborg, Denmark
[3] Department of Chemistry and Food Chemistry, Center for Advancing Electronics Dresden (cfaed), Technische Universität Dresden, 01062 Dresden, Germany
[4] Laboratory of Bio-Inspired and Graphene Nanomechanics, Department of Civil, Environmental and Mechanical Engineering, University of Trento, via Mesiano 77, I-38123 Trento, Italy
[5] Sixonia Tech GmbH, Pestitzer Str. 16, 01187 Dresden, Germany
[6] School of Engineering and Materials Science, Queen Mary University of London, Mile End Road, London E1 4NS, UK

Controllable rapid expansion and activation of gases is important for a variety of applications, including combustion engines, thrusters, actuators, catalysis, and sensors. Typically, the activation of macroscopic gas volumes is based on ultra-fast chemical reactions, which require fuel and are irreversible. An "electrically powered explosion", i.e., the rapid increase in temperature of a macroscopic relevant gas volume induced by an electrical power pulse, is a feasible repeatable and clean alternative, providing adaptable non-chemical power on demand. Till now, the fundamental problem was to find an efficient transducer material that converts electrical energy into an immediate temperature increase of a sufficient gas volume. To overcome these limitations, we developed electrically powered repeatable air explosions (EPRAE) based on free-standing graphene layers of nanoscale thickness in the form of microtubes that are interconnected to a macroscopic framework. These low-density and highly permeable graphene foams are characterized by heat capacities comparable to air. The EPRAE process facilitates cyclic heating of cm^3-sized air volumes to several 100 °C for more than 100,000 cycles, heating rates beyond 300,000 K s^{-1} and repetition rates of several Hz. It enables pneumatic actuators with the highest observed output power densities (>40 kW kg^{-1}) and strains ~100%, as well as tunable microfluidic pumps, gas flowmeters, thermophones, and micro-thrusters.

Introduction

Explosions, although generally considered destructive, offer an efficient way to convert potential (usually chemical) energy into kinetic energy in a gas within a short time [1,2]. In general, an explosion is defined as the sum of the phenomena that occur during a local rapid release of energy. In addition, the release of energy must be sufficiently rapid and concentrated to produce an audible pressure wave [3]. The released energy is locally converted into a temperature rise causing an overpressure, leading

* Corresponding authors.
E-mail addresses: Schütt, F. (fas@tf.uni-kiel.de), Adelung, R. (ra@tf.uni-kiel.de).
† Shared first authorship.

https://doi.org/10.1016/j.mattod.2021.03.010

to an excess energy density that is degraded through heat transport and volume work in the environment [1,2].

However, even though such chemical explosions are widely used, they always require fuel and are irreversible [4], as fuel is consumed. In contrast to that, an "electrical explosion", i.e., the rapid increase in temperature of a macroscopic gas volume induced by an electrical power pulse, could be a feasible repeatable and clean alternative. Till now, the fundamental problem was to find a suitable transducer material, fulfilling the following criteria: (I) high and open porosity in order to contain large gas volumes (II) rapid volumetric Joule heating (coefficient of performance of ~1.0 [5]) with rates well beyond 100,000 K s^{-1}, (III) rapid (~ms) heat transfer from the transducer material to a large gas volume provided by a high volumetric surface area and (IV) resistance to high temperatures (up to several 100 °C) and temperature fluctuations. Additionally, (V) the volumetric heat capacity of the transducer material needs to be in the order of that of gases to allow for sufficiently fast heating and cooling rates and, therefore, high frequencies (explosions per second). Traditional Joule-heating technologies, such as radiant heaters, convection heaters, or fan heaters, do not fulfil all the described requirements, as they are typically based on bulk metal wires.

Recently, macroscopic three-dimensional (3D) carbon nanomaterial assemblies have been shown to hold great promise for Joule heating applications [6–8], e.g., gas sensing [9], throughflow heaters [10], loudspeakers [11–13], air filtration [14], bolometers [15], or clean-up of viscous crude oil [16]. They offer the possibility to utilize the exceptional properties of carbon nanomaterials, such as graphene [17], on the macroscopic scale, while not being limited by any underlying substrate [18]. However, with reported heating rates in the order of 10 K s^{-1} and an unfavorable nano- and microstructural arrangement of the used carbon nanomaterials assemblies (i.e., Knudsen Number ≥ 1), they were far from fulfilling the above-mentioned criteria needed for an efficient transducer material that is capable of carrying out a multitude of electrically powered explosions.

Here, we use graphene-based framework–aeromaterials (F-AMs) for electrically powered repeatable air explosions (EPRAE), with heating, cooling, and repetition rates of ~10^5 K s^{-1}, ~10^4 K s^{-1}, and ~10 Hz, respectively (Fig. 1). As illustrated in Fig. 1a, the employed F-AMs feature an interconnected network of hollow exfoliated graphene (EG) or reduced graphene oxide (rGO) microtubes with a nanoscopic wall thickness (<25 nm) [19]. The open-porous (~99.9%) structure and low density (~2–20 mg cm^{-3}) of the F-AMs result in an ultra-low volumetric heat capacity (between 1 to 5 kJ m^{-3} K^{-1}, Supplementary Text S1) similar to that of air, a high and fully accessible volumetric surface area (~0.14 m^2 cm^{-3}, Supplementary Text S2), and mechanical robustness [19,20], in which the properties of the gaseous phase can be estimated to that of free gas (Knudsen number $\ll 1$). This extraordinary set of properties of the F-AMs forms the basis of the EPRAE concept.

The idealized thermodynamic processes of the EPRAE concept are schematically illustrated in Fig. 1b. While air was used as the working gas in this study, the concept is also valid for other gases, such as nitrogen or argon. In the first step (state 1 → 2), heat is rapidly and uniformly transferred to the gas contained inside the F-AMs by fast (<1 ms) Joule heating of the F-AMs. This results in a fast increase in the kinetic energy of the gas molecules contained inside the F-AMs and, thus, an increase in the pressure of the system. The second step (state 2 → 3) involves a rapid (~1 ms) adiabatic expansion of the gas back to the equilibrium pressure (the actual explosion), followed by an isobaric heat rejection (state 3 → 1) to the starting volume and temperature in around 200 ms. Such a thermodynamic cycle is also referred to as the Lenoir cycle [21], which is used as a model to describe the thermodynamics of the first commercially produced combustion engine, invented in 1860. A series of several EPRAEs can be seen (and heard) in the Video S1.

While a fast heat transfer from the F-AMs to the gas is given by their large volumetric surface area, the open-porous framework structure is key for the EPRAE concept, as it allows for a fast heat transfer by convection and, thus, rapid (<10 ms) and large (e.g., 200%) volume expansions, without causing any structural damage to the F-AMs during operation. In contrast to conventional gas activation systems, such as blowers, gas pumps, fans, heating wires or hotplates, the EPRAE concept enables the rapid activation of arbitrarily scalable gas volumes (from litres to nanolitres), based on the size of the F-AM and the amount of electrical energy used. Additionally, as no chemical reaction is involved, the process is environmentally friendly, repeatable and can be conducted with relatively low voltages/currents and high repetition rates (~10 Hz) as a sequence of explosions (Fig. 1c, corresponding voltage/current profiles in Fig. S1). We demonstrate that EPRAE can be exploited for different applications, such as the fabrication of a novel class of fluidic pumps (e.g., for microfluidic systems), extremely fast pneumatic micro and macro actuators (e.g., for soft robotics, tactile displays, shock absorber systems), thermophones, micro-thrusters, as well as highly sensitive gas flowmeters.

Results and discussion

Fabrication and characterization of F-AMs

The employed F-AMs were fabricated as described elsewhere [19,22] (Materials and Methods and Supplementary Figs. S2 and S3). In short, highly porous (~94%) networks of interconnected tetrapod-shaped zinc oxide (t-ZnO) microparticles [23] (Fig. S2) were infiltrated with water-processable EG or graphene oxide (GO) dispersions, resulting in a homogenous coating of the template material with a thin (<25 nm) layer of the nanomaterials. Afterwards, the t-ZnO templates were removed by HCl etching and the GO-based samples were chemically reduced with ascorbic acid to obtain rGO networks. Finally, the samples were washed with deionized water and transferred to absolute ethanol for critical point drying (Fig. S3).

The resulting macroscopic structures have a cylindrical geometry with high uniformity in size (6 mm in diameter and height) and consist of a network of interconnected hollow microtubes with a mean length of ~25 μm, a diameter of ~2 μm and a wall thickness of ~25 nm, as shown in Fig. 2a and b. It should be noted that a large fraction of the microtubes does not completely retain the hexagonal morphology of the ZnO tetrapod arms and shows a more roundish shape after etching and drying (Fig. 2b). However, this does not affect the mechanical integrity and the microstructure of the samples. In the following, the F-AMs pro-

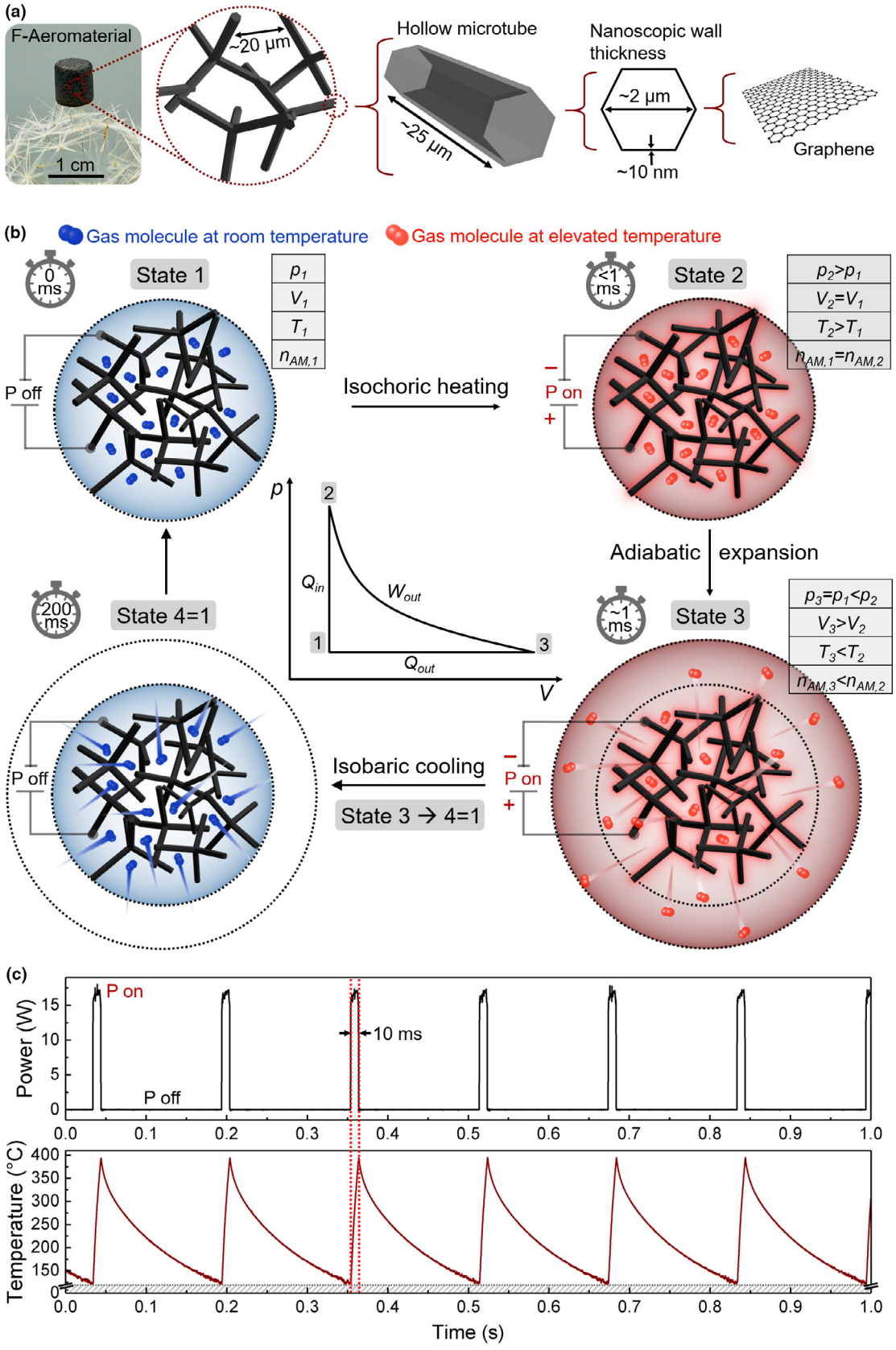

FIGURE 1

Electrically powered repeatable air explosions (EPRAE). (a) Photograph of highly porous (99.9%) graphene-based framework aeromaterial (F-AM), consisting of interconnected, hollow graphene microtubes (~25 μm in length, ~2 μm in diameter) with nanoscopic wall thickness (~10 nm). (b) Idealized thermodynamic cycle of the EPRAE concept, involving an isochoric rapid (<1 ms) heat addition to the gas (state 1 → 2) by Joule heating of the F-AMs causing a pressure increase, followed by a rapid adiabatic expansion of the gas (state 2 → 3) back to its original pressure and a final isobaric heat rejection (state 3 → 1) to its original volume and temperature. Please note that the schematic is not to scale – the size of the molecules is several orders of magnitude smaller than the pore size of the F-AM. (c) Typical EPRAE temperature–time profile (bottom), induced by 10 ms power pulses (peak power ~18 W) at a repetition rate of ~6.7 Hz (top).

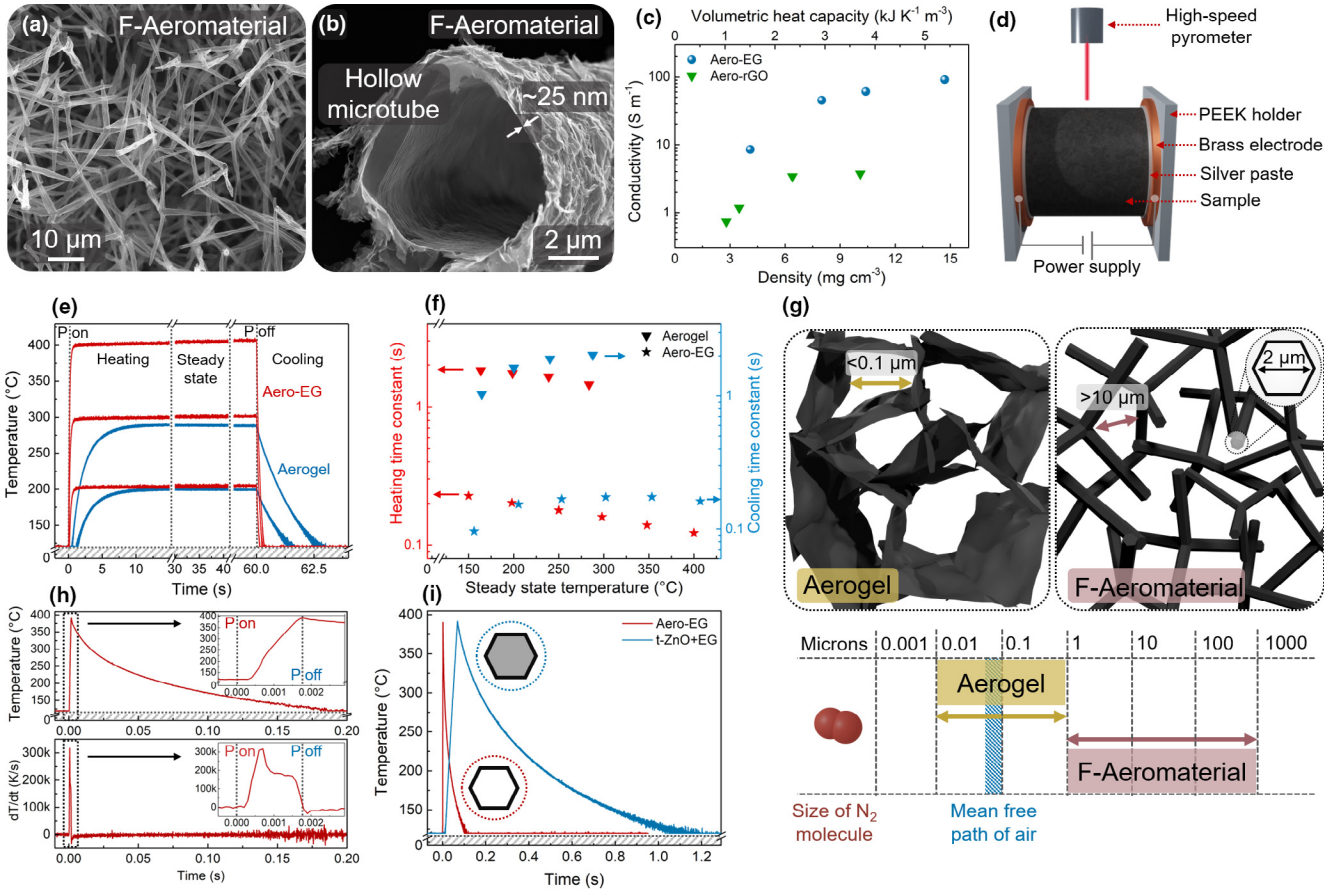

FIGURE 2

Microstructure and properties of F-AMs. (a) and (b) Representative SEM images of the F-AMs, revealing the framework structure with hollow, interconnected microtubes and high open porosity. (c) Conductivity versus F-AM density/volumetric heat capacity for Aero-EG and Aero-rGO. (d) Schematic of setup for investigation of Joule-heating and cooling characteristics of the F-AMs and the graphene aerogel. (e) Steady-state Joule-heating and cooling characteristics of Aero-EG and a graphene aerogel for different applied powers (details in Fig. S7). (f) Heating and cooling time constants for Aero-EG and the aerogel, obtained from the steady-state Joule-heating temperature–time profiles shown in e and Fig. S6. (g) Schematic of the structural morphologies of a typical graphene aerogel and a F-AM, respectively. As denoted in the diagram, the length scales of the pore sizes in the F-AM are more than two orders of magnitude larger than the mean free path of air, whereas the latter is in the same order or above typical pore sizes in the aerogel. (h) Non-steady-state Joule-heating and cooling characteristics of Aero-EG after inducing a short (1.7 ms) power pulse (152 W), showing the temperature–time profile (top) and its derivative (bottom). The latter shows the heating and cooling rates as a function of time. (i) Comparison of temperature–time profiles for Aero-EG and EG-coated t-ZnO network after inducing short power pulses to the samples (2.1 ms and 69.2 ms).

duced from rGO and EG are labeled as Aero-rGO and Aero-EG, respectively. The electrical conductivity of the F-AMs can be adjusted by increasing the amount of deposited EG and GO flakes on the sacrificial templates. Fig. 2c shows that the electrical conductivity of Aero-EG and Aero-rGO increased almost linearly with the density, reaching maximum values of around 90 S m^{-1} and 3 S m^{-1} for Aero-EG (14 mg cm^3) and Aero-rGO (10 mg cm^3), respectively. The higher conductivity of Aero-EG indicates the high quality of the employed EG sheets, which is also confirmed by the low D/G band intensity ratio determined by Raman microscopy (Fig. S4).

Steady-state Joule-heating and cooling characteristics of F-AMs

The Joule-heating and cooling characteristics of the F-AMs were investigated by a high-speed pyrometer working in the temperature range between 120 °C and 550 °C (more details in Materials and Methods). As schematically shown in Fig. 2d, the F-AMs were contacted with conductive silver paste between two brass electrodes and placed in the focus of the pyrometer. To investigate the complete temperature range during Joule heating and cooling of the F-AMs, the temperature profiles were additionally measured with an infrared camera (Figs. S5 and S6). Fig. 2e demonstrates the difference in the steady-state Joule heating characteristics of both Aero-EG and a classical graphene aerogel (prepared via chemical reduction of a GO dispersion [24], details in Materials and Methods) for different applied input powers (1–5 W) over a time period of one minute. The steady-state temperature of Aero-EG increases almost linearly with applied input power (Fig. S7), with a heating performance (dT dP^{-1}) of 83 K W^{-1}, similar to what was reported for carbon nanomaterial thin film heaters [25,26] and aerogels [6]. Additional temperature profiles for Aero-rGO, Aero-EG, and the aerogel are shown in Fig. S7 together with the corresponding heating performance. The difference in the Joule-heating and cooling behavior of the F-AMs and the graphene aerogels in Fig. 2e is best described by

their thermal time constants (τ_H for heating and τ_C for cooling) as a function of steady-state temperature, Fig. 2f (more details in Fig. S8 and Supplementary Text S3). Both τ_H and τ_C were around one order of magnitude lower for the F-AMs when compared to the classical aerogels, with values on the order of 10^{-1} s, even though their density (~10 mg cm^{-3}), electrical conductivity (~30 S m^{-1}) as well as volumetric heat capacity (~3 kJ m^{-3} K^{-1}, Supplementary Text S1) are on the same order of magnitude. The differences in τ_H and τ_C are directly related to the dissimilar micro- and nanostructure of the F-AMs compared to the aerogels (Fig. 2g and SEM images in Fig. S9), which strongly affects the heat transport within the structures. In general, the heat transport within non-evacuated porous materials is based on three mechanisms [27]: (I) heat conduction via the solid backbone, (II) diffusive heat transfer within the gaseous phase present in the open-porous structure, and (III) radiative heat transfer. The heat transfer through the carbon backbone of highly porous graphene aerogels has been shown to be extremely low, with thermal conductivities equivalent to 80% of air [28]. Furthermore, the radiative heat transfer in carbon nanomaterial aerogels is negligible [27]. Thus, heat transfer by the diffusion of gases is the dominant mechanism, which is characterized by the Knudsen number (Kn):

$$Kn = \frac{l_g}{D} \quad (1)$$

where l_g denotes the mean free path length of gas molecules and D is the effective pore dimension [27,29]. At standard pressure and room temperature, the mean free path of air is close to 68 nm [30]. In the case of classical graphene aerogels, the nanosheets are homogenously dispersed throughout the macroscopic volume with characteristic pore sizes well below the micron range (schematic in Fig. 2g), yielding values of Kn close to 1. Therefore, the heat transfer via the gaseous phase is strongly reduced within the aerogel. In contrast, in the case of the here employed F-AMs, the nanosheets are inhomogeneously distributed throughout the entire volume in the form of hollow microtubes, with a mean distance between the individual elements (hollow microtubes) of several tens of micrometers. The framework morphology of the F-AMs results in $Kn \ll 1$, since the mean free path of the gas molecules is 2–3 orders of magnitude smaller than the effective pore size [30]. The heat transfer in the F-AMs can, thus, be approximated by that of the free gas, with the gas molecules predominantly colliding with each other [27]. The almost undisturbed heat transfer via the gaseous phase enables the F-AMs to reach steady-state Joule-heating conditions almost instantaneously, resulting in mean heating and cooling rates superior to that of classical aerogels [6] by at least one order of magnitude (Fig. S10). All in all, the combination of several structural properties is important to realize the demonstrated fast heating and cooling rates, including a low volumetric heat capacity similar to that of the surrounding gas, a high and open porosity, and an appropriate distance between the carbon-based structural elements which act as heating elements.

Electrically powered repeatable air explosions (EPRAE)

These characteristics enable the F-AMs to be used as an efficient transducer material capable of rapidly converting electrical energy into heat of cm^3-sized gas volumes at high repetition rates, resulting in electrically powered repeatable air explosions (EPRAEs). The corresponding Joule-heating and cooling characteristics of the EPRAE process were characterized by applying short (1 ms up to 100 ms) power pulses to the F-AMs. Fig. 2h (top) shows the temperature–time profile of an Aero-EG sample (density ~8 mg cm^{-3}, conductivity ~35 S m^{-1}) induced by a 1.7 ms power pulse width of 640 W cm^{-3} peak power under ambient conditions. The short power pulse resulted in a temperature increase from room temperature (RT) to around 390 °C, while cooling to 120 °C (limit of pyrometer) took around 190 ms. The corresponding heating and cooling rates (dT dt^{-1}) are depicted in Fig. 2h (bottom), with maximum values of 317,000 K s^{-1} and 40,000 K s^{-1}, respectively, which are 4 orders of magnitude higher compared to previous reports [6,10,16]. As revealed by the insets in Fig. 2h, there are three different regimes in the heating phase (0–1.7 ms). At first, the heating rate approaches a maximum after around 0.7 ms, followed by an almost constant plateau at ~190,000 K s^{-1} and a further steep decline at 1.6 ms, before the power is turned off. The different regimes correspond to the isochoric heating phase and the subsequent adiabatic gas expansion (refer to Fig. 1b). Furthermore, the heating rate can be adjusted by tuning the applied power pulse width (PPW). In Fig. S11, the Joule-heating characteristics of the F-AMs at constant energy input are shown for different power pulse durations.

In addition to the open-porous framework structure of the F-AMs, their extremely low volumetric heat capacity is crucial for the EPRAE process. To demonstrate that, we carried out comparative measurements between an Aero-EG sample (~4 mg cm^{-3}) and an EG/ZnO (~300 mg cm^{-3} / ~4 mg cm^{-3}) sample (non-etched EG-coated t-ZnO template), as shown in Fig. 2i. Both samples had a conductivity of ~8 S m^{-1}. The volumetric heat capacity of the Aero-EG can be estimated to be around ~6 kJ m^{-3} K^{-1} (Supplementary Text S1) while that of Aero-EG/ZnO is in the order of ~155 kJ m^{-3} K^{-1} and, thus, by a factor of ~26 higher. While heating of Aero-EG to 390 °C was achieved within 2.1 ms using an energy density of ~0.7 J cm^{-3}, a much higher energy density of ~14 J cm^{-3} (factor of 20) was required to heat the Aero-EG/ZnO sample to the same temperature. The large difference in the volumetric heat capacity can be best observed with respect to the cooling characteristics. While it takes only around 100 ms for Aero-EG to cool to 120 °C, the cooling of the EG/ZnO is by a factor of 10 longer (~1050 ms). Even slight changes in the density and, therefore, volumetric heat capacity of the F-AMs affect their heating and cooling characteristics and, thus, the EPRAE process (Supplementary Text S4).

Long-term stability of F-AMs during EPRAE

We further carried out long-term EPRAE measurements of up to 100,000 cycles between < 120 °C (limit of pyrometer) and ~400 °C as well as long-term (~12 h) steady-state measurements for different temperatures (Figs. S12 to S14) in order to study the stability of the F-AMs under these conditions. As shown in Fig. 3a, an Aero-rGO sample with a density of ~4 mg cm^{-3} is stable over 100,000 cycles (repetition rate 1 Hz) when subjected to a power pulses with a 1.5 ms PPW and a peak power density of ~200 W cm^{-3}, reaching a maximum temperature of 400 °C.

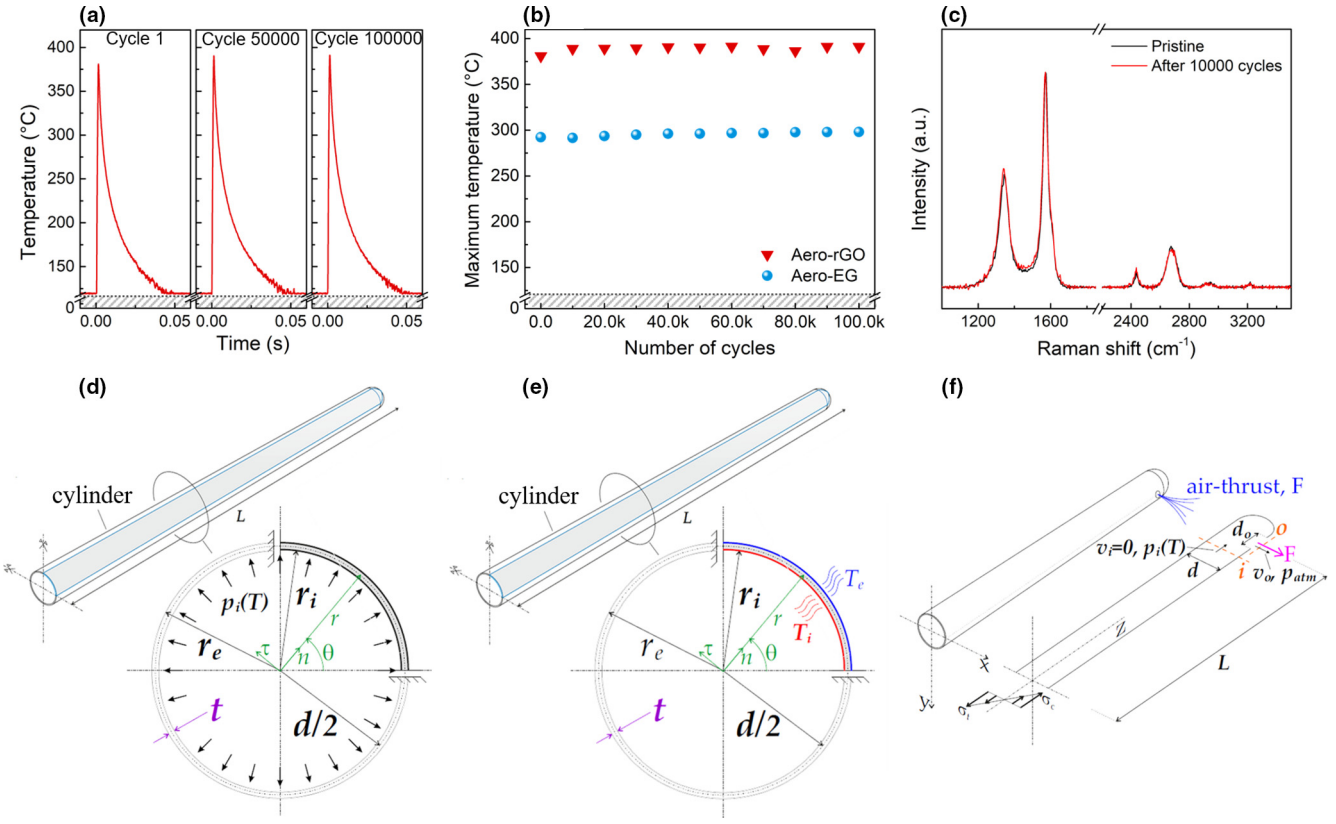

FIGURE 3

Long-term stability of EPRAE. (a) Temperature-time profiles for Aero-rGO (~4 mg cm^{-3}) during repetitive Joule-heating and cooling cycles, shown for the cycle 1, 50,000, and 100,000. (power pulse width = 1.5 ms; peak power density ~200 W cm^{-3}; repetition rate ~1 Hz.) (b) Evolution of maximum temperature over 100,000 EPRAE cycles, shown for Aero-rGO and Aero-EG. (c) *In situ* Raman spectra of Aero-EG before and after 10,000 EPRAE cycles. (d)–(f) Schematic of the analyzed failure mechanisms that could cause destruction of the F-AMs by the EPRAE process, i.e., (d) Hoop and longitudinal stress generated by air expansion inside the microtubes, (e) thermal stress caused by a temperature gradient between the inner and outer temperature of the microtube wall, and (f) longitudinal stress caused by airflow through the microtube voids.

The maximum temperature remained constant (Fig. 3b) and no change in the heating and cooling characteristics could be observed (Fig. 3a), indicating excellent long-term stability of Aero-rGO during EPRAE. Similarly, Aero-EG (density ~11 mg cm^{-3}) showed cycling stability over 100,000 cycles at a maximum temperature of ~300 °C and PPW of 1.3 ms (peak power density of ~190 W cm^{-3}), revealing constant heating and cooling characteristics (Fig. S12) as well as a constant maximum temperature (Fig. 3b). A photograph and SEM images of Aero-EG after 10,000 EPRAE cycles is presented in Fig. S15 and demonstrates the preservation of the macroscopic and microscopic structure. Additionally, *in situ* Raman measurements of Aero-EG demonstrated high chemical stability during cyclic Joule heating, as only minor changes in the spectra could be observed (Fig. 3c and Fig. S16). It should be noted that, despite its higher temperature stability compared to Aero-rGO, long-term EPRAE cycling of Aero-EG at 400 °C resulted in failure of the sample after a few 1000 cycles, evident by a temperature increase and change in cooling time (Fig. S13). We suspect that the lower stability of Aero-EG during EPRAE is caused by its lower mechanical stability compared to Aero-rGO [19]. The long-term constant Joule-heating characteristics (constant heating for a time period of 12 h) of Aero-rGO and Aero-EG are presented in Fig. S14.

Possible thermo-mechanical failure mechanisms resulting in the destruction of individual microtubes caused by the rapid heating of the F-AMs were investigated by analytical calculations and numerical simulations. In particular, three mechanisms have been identified (Fig. 3d–f): (M1) Hoop and longitudinal stress generated by a rapid air expansion inside the microtubes resulting in a pressure difference between the inside and the outside of the microtube (Fig. 3d), (M2) thermal stress caused by a temperature gradient between the inner and outer temperature of the microtube wall (Fig. 3e), and (M3) longitudinal stress caused by airflow through the microtube voids. The mechanisms are thoroughly discussed and analyzed in the Supplementary Information (Figs. S17 to S21 and Supplementary Text S5). The numerical and theoretical results suggest that the hollow microtubes most likely break by a combination of the mechanisms M1 and M2. The latter mechanism is suspected to be mainly responsible, with a Tresca maximal strength (shear strength) of the microtube on the order of 2–3 GPa, depending on the geometrical configuration (Tables S1–S4). We emphasize that the predicted stress is independent from the Young's modulus for the mechanism (A) and linearly dependent for the mechanism (B). Therefore, we suspect that the rapid volume expansions caused by the extremely fast temperature changes result in a structural damage (i.e., breaking of microtubes) over time. At constant volt-

age, a higher current will pass through the remaining microtubes of the F-AM network, causing an overall higher temperature and finally failure due to oxidation reactions. At even more extreme heating rates of $\sim 4 \cdot 10^6$ K s^{-1} (50 µs power pulses of 576 W, ΔT ~200 K) the complete F-AM starts to disintegrate, with macroscopic parts being pushed out from the structure, as shown in Video S2.

Rapid gas activation based on EPRAE

To obtain a deeper insight into the thermodynamic processes of individual EPRAEs, we measured the air volume expansion under isobaric conditions as well as air pressure changes under isochoric conditions as a function of the PPW. Therefore, an electrically connected F-AM was mounted into an air-tight chamber. For the isobaric system, two check valves were attached to the

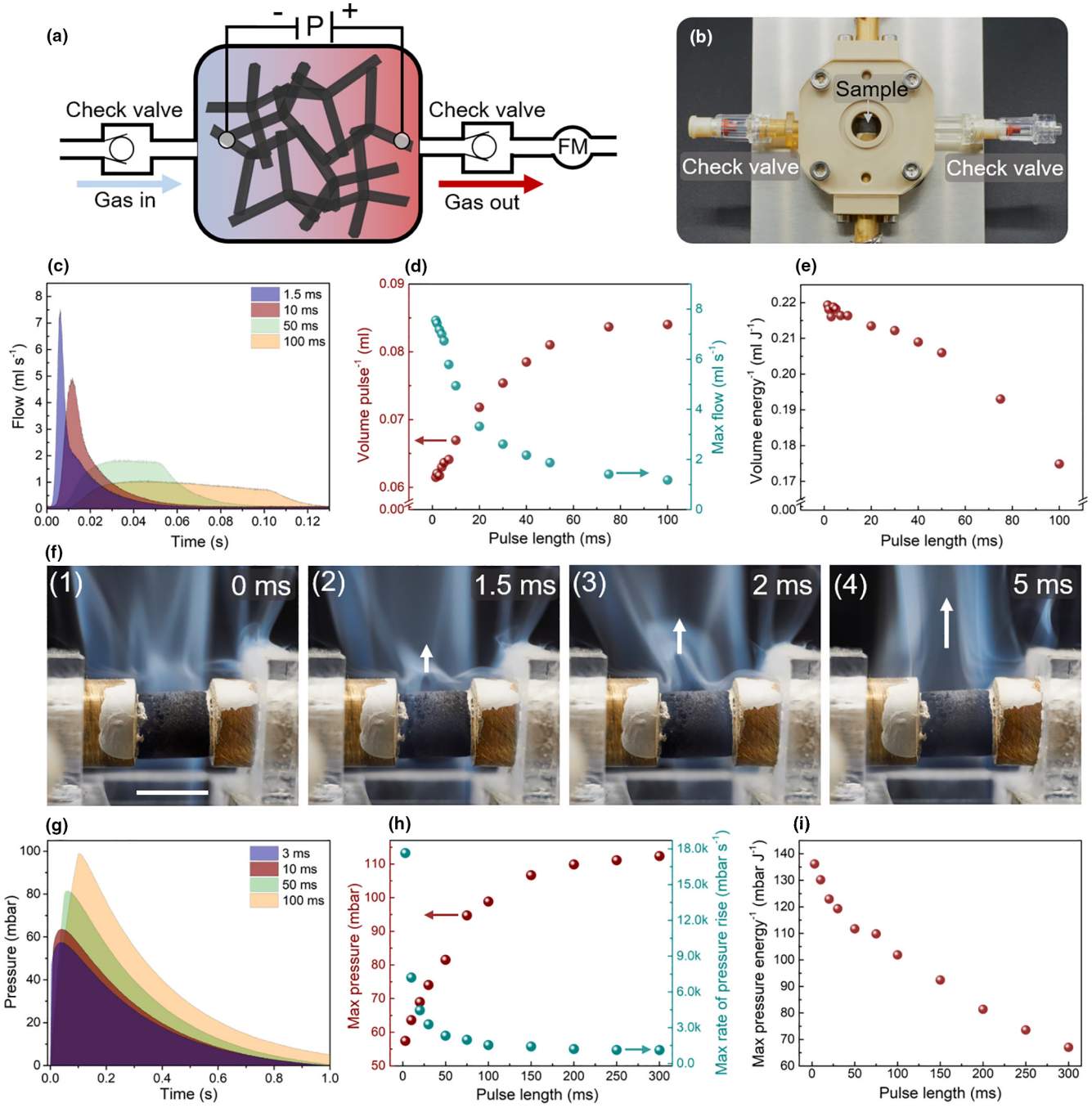

FIGURE 4

Rapid gas activation based on EPRAE. (a) Schematic of the measurement setup for the determination of the air volume expansion caused by EPRAE (P: power; FM: gas flow meter). For the pressure measurement, the right check valve and the flow meter were replaced by a pressure sensor. (b) Photograph of the employed measurement setup. (c) Air flow versus time for Aero-EG, resulting from EPRAEs to 400 °C at four different power pulse widths (PPWs). (d) Activated air volume per pulse and maximum air flow versus PPW. (e) Activated air volume normalized to the supplied energy versus PPW. (f) Sequence of photographs showing the EPRAE process. After applying a 1.5 ms power pulse to the sample, the heated air inside the F-AM expanded rapidly and displaced the surrounding smoke (white arrow) produced by an incense stick. Scale bar: 6 mm. (g) Pressure versus time for Aero-EG, resulting from EPRAEs to 350 °C at four different PPWs. (h) Maximum pressure and maximum rate of pressure rise versus PPW. (i) Maximum pressure normalized to the supplied energy versus PPW.

chamber to ensure air flow in only one direction (Fig. 4a and b). Thermodynamically, in case of an isobaric process, an increase in gas temperature is directly related to an increase in gas volume. In the given setup, the increase in air volume caused by an EPRAE induces an air flow through the right check valve, which is measured by a gas flow meter connected in series. The left check valve ensured pressure equalization after each heating pulse. The air flow induced by individual EPRAEs was measured as a function of PPW (1.5–100 ms), as shown in Fig. 4c. The maximum temperature was kept constant at 400 °C by adjusting the applied pulse power (Fig. S22). In the case of a pulse time of 1.5 ms, the air flow reaches a maximum of ~7.5 ml s^{-1}. As soon as the power is switched off, the air flow decreases rapidly to 0 (~70 ms). Increasing the PPW results in a decrease in the maximum air flow but a longer overall air flow, as shown in Fig. 4c. With increasing PPW, the maximum air flow decreases from ~7.5 ml s^{-1} to ~1.6 ml s^{-1}, while the activated air volume per pulse increases from ~0.065 ml to ~0.085 ml, at 1.5 ms and 100 ms PPW, respectively (Fig. 4d). For PPWs > 75 ms, the volume per pulse approaches an upper limit of 0.085 ml. Assuming ideal gas behavior, the air contained inside the F-AM (volume ~0.16 ml) should expand to a volume ~0.37 ml at a temperature change from 20 °C to 400 °C, causing a total air flow of ~0.21 ml. Considering the upper limit of 0.085 ml, the efficiency of the system is ~41 %. The detailed calculation of the pump efficiency is presented in the Supplementary Text S5.

We suppose measured value of 0.085 ml is caused by the fact that the bulky metal contacts act as a heat sink, resulting in lower heating of the sample close to the contact surface, similar to what was reported for the heating of other carbon nanomaterial assemblies [6]. Additionally, an optimized experimental setup could contribute to an increased efficiency. Nevertheless, the measurements demonstrate that a large part of the gas contained inside the F-AMs can be rapidly and reversibly activated by the EPRAE process, e.g. ~40% in 1.5 ms. Activating a higher percentage would be possible by further increasing the surface area or the density of the F-AMs. However, this would have direct consequences on the gas transport inside the F-AMs during EPRAE (see Supplementary Text S4). With respect to energy consumption, the EPRAE process is more efficient the lower the PPW (Fig. 4e), with a maximum value of ~0.22 ml J^{-1} at 1.5 ms. With increasing PPW, the value decreases to ~0.17 ml J^{-1} for 100 ms PPW. This behavior can be understood as follows. In the first heating stage the gas close to the microtubes of the F-AMs is rapidly heated. Heating of the gas volume further away from the microtubes is accomplished by heat transfer within the gaseous phase, which requires more time compared to the heating of the initial gas volume. The air expansions caused by a 1.5 ms EPRAE to ~400 °C is visualized in the photographs shown in Fig. 4f (and Video S1). The smoke (produced by an incense stick) surrounding the F-AM is rapidly pushed away by a single EPRAE.

We further investigated the change in air pressure caused by individual EPRAEs in the chamber by replacing the right check valve by a pressure sensor, providing an isochoric system. Thermodynamically, in case of an isochoric process, an increase in gas temperature scales linearly with an increase in gas pressure, as shown in Fig. S23 for a F-AM, which was heated to different temperatures between 150 °C and 400 °C at a constant PPW. The obtained pressure–time curves for different PPWs (3–100 ms) are shown in Fig. 4g. Please note that the shortest PPW is slightly longer (3 ms) compared to the air flow measurement shown in Fig. 4c (1.5 ms). This is due to the use different samples with slightly differing resistances and the limitation of the voltage supply (29 V), resulting in small differences in the shortest possible time to heat the samples to ~400 °C. The maximum temperature was kept constant at 350 °C by adjusting the applied power (Fig. S22). In the case of 3 ms PPW, the air pressure in the chamber reached a maximum of ~56 mbar (in addition to the standard pressure). As soon as the power was switched off, the pressure decreased down to its original value (~1 s). Increasing the PPW of the EPRAE resulted in an increase in the maximum pressure, e.g., 104 mbar at 300 ms PPW (Fig. 4h). For PPWs > 150 ms, the maximum pressure approached an upper limit. The slight increase in maximum pressure for PPWs > 150 ms is most likely caused by the heating of the air surrounding the F-AM. The maximum rate of pressure rise, a number used to describe explosions, decreased with increasing PPW (Fig. 4h), with a maximum value of ~18 bar s^{-1} for a PPW of 3 ms. In Fig. 4h, the maximum pressure is plotted as a function of supplied energy, indicating that shorter EPRAE PPWs are more efficient. The results are in accordance with the once obtained from the measurements under isobaric conditions.

Applications of EPRAE

The measurements shown in Fig. 4 demonstrate that the EPRAE process enables ultrafast (few ms) and repeatable activation of macroscopic gas volumes, which can be exploited for a broad variety of applications (Fig. 5), such as micro-pumps for fluidics, rapid micro-actuators, micro-thrusters, as well as thermophones. Fig. 5a shows a schematic of the different working principles. As shown in Fig. 5b, a rapid succession of EPRAEs at a repetition rate of 6.25 Hz was exploited to pump a fluid through a glass capillary. The corresponding flow rate versus time profile is shown in Fig. 5c. As revealed by the magnification between 5 and 6 s in Fig. 5d, peak values of 400 °C and 160 ml min^{-1} were obtained for the temperature and air flow, respectively. The corresponding Video S3 shows the step-like movement of the fluid, where each step represents an individual heating pulse. The pumping rate of the micro-pump can be controlled by changing the EPRAE process parameters. It is proportional to the change in temperature (and, thus, power), the repetition rate (power pulse frequency), and the power pulse width and can be tuned on the fly. An almost constant gas flow of 9 ml min^{-1} (~60 ml min^{-1} cm^{-3} normalized to the volume of the F-AM) could be achieved by cycling the system between ~400 °C and ~200 °C at a 5 ms power pulse duration and frequency of ~9.5 Hz (Fig. S24). In contrast to conventional miniature gas pumping systems, which rely on oscillating membranes, our system is free of any mechanical moving parts (except for the check valves). Furthermore, existing gas pumping systems that do not require mechanical moving parts, such as Knudsen pumps [31] (thermal transpiration pump), usually have very low specific pumping rates on the order of ~0.03 ml min^{-1} cm^{-3} [31], a factor of ~2000 lower compared to what is reported here. In terms of energy consumption, the EPRAE-based pump outperforms Knudsen pumps by 2 orders of

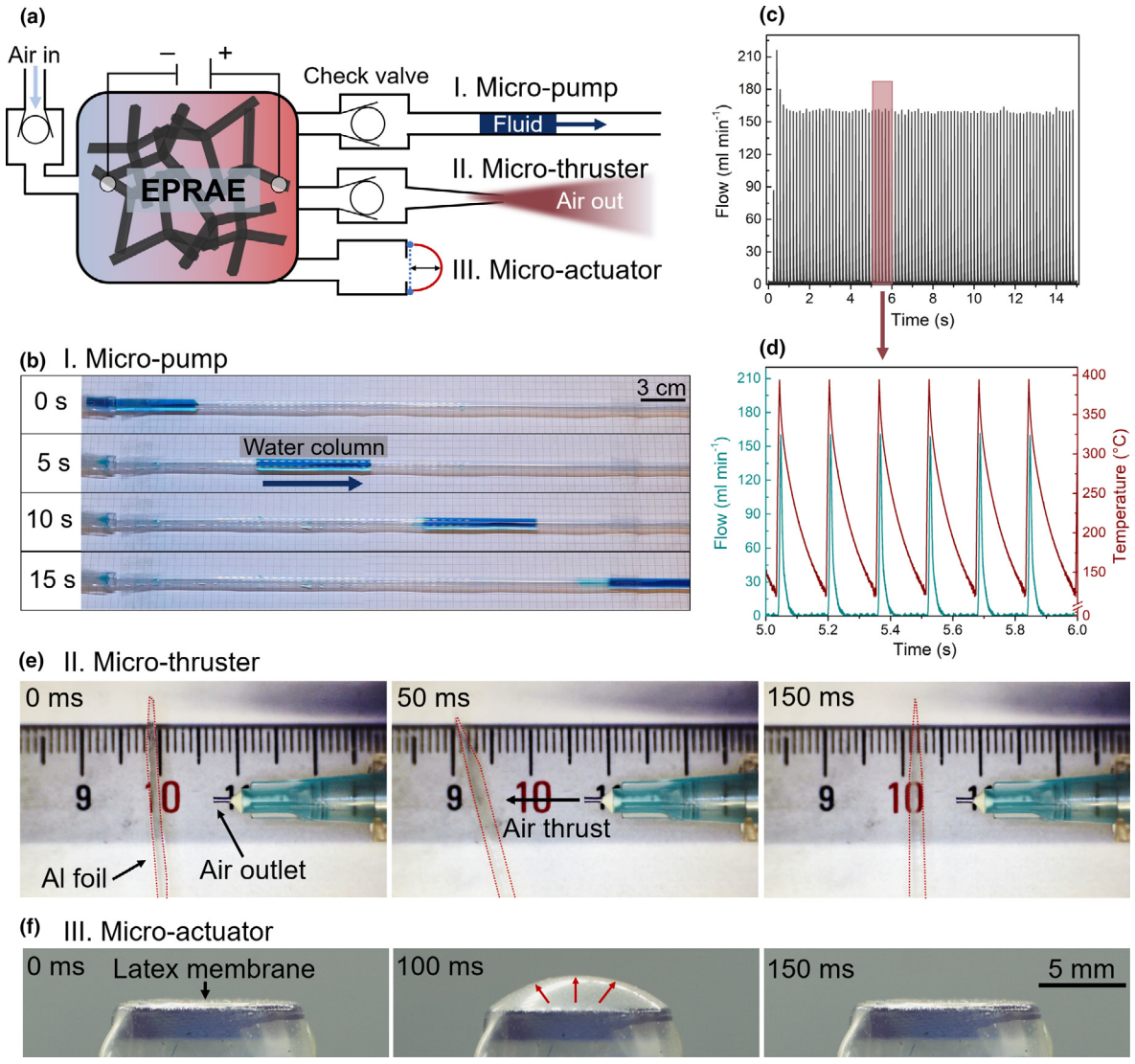

FIGURE 5

EPRAE Applications. (a) Schematic illustration of three EPRAE applications: I. micro-pump, II. Micro-thruster and III. Micro-actuator. The corresponding videos of the applications are shown in Video S3. (b) Sequence of photographs showing the exploitation of a sequence of EPRAEs for pumping a fluid through a glass capillary. (c) Corresponding air flow versus time to the photographs shown in B. The EPRAE repetition rate is 6.25 Hz with a peak power of ~16.5 W and a PPW of 10 ms. The range between 5 and 6 s is magnified in (d) and complemented by the corresponding temperature–time profile. (e) Sequence of photographs showing the rapid creation of an air thrust moving a thin aluminum foil induced by a single EPRAE (PPW of 50 ms, peak power ~26.5 W) A photograph of the setup is shown in Fig. S23. (f) Sequence of photographs showing the rapid micro-actuation of a rubber membrane, induced by a single EPRAE (PPW of 100 ms, peak power ~10 W).

magnitude, with ~0.47 ml min^{-1} cm^{-3} W^{-1} and ~51.25 ml min^{-1} cm^{-3} W^{-1}, respectively. In addition to microfluidic pumping systems, the explosion-like air expansion produced by EPRAE can also be employed in the scope of lightweight, highly precise and rapid micro-thrusters (Fig. 5e and Video S3, photograph of setup in Fig. S25), e.g., for the use in resistojets for micro propulsion systems of satellites [32]. Same as for the micropumps, the thrust can be controlled by the EPRAE process parameters. Based on their low volumetric heat capacity and microstructure, the demonstrated F-AMs are also ideal candidates for omnidirectional thermophones. As shown in Fig. S26A and Video S3, a common in-ear headphone casing was equipped with a F-AM (cylindrical geometry with a diameter of 6 mm and a height of 5 mm) to emit sound over a broad frequency range by using a conventional tablet. The change in temperature for different applied frequencies can be seen in Fig. S26B, indicating that even high frequencies of 500 Hz induce large temperature fluctuations of more than 2 K. These properties can also be used for highly sensitive gas flow meters showing an exponential decay of the maximum temperature with increasing gas flow (details in Fig. S27), as even small air movements such as clapping have a direct effect on the temperature of the F-AMs (Video S5).

Furthermore, the EPRAE concept can be used for the fabrication of rapid, lightweight and repeatable pneumatic micro- and macro-actuators, that do not require any external pressure source, which makes them highly interesting for soft robotics [33–35]. As shown in Fig. 5f and Video S3, a thin latex membrane

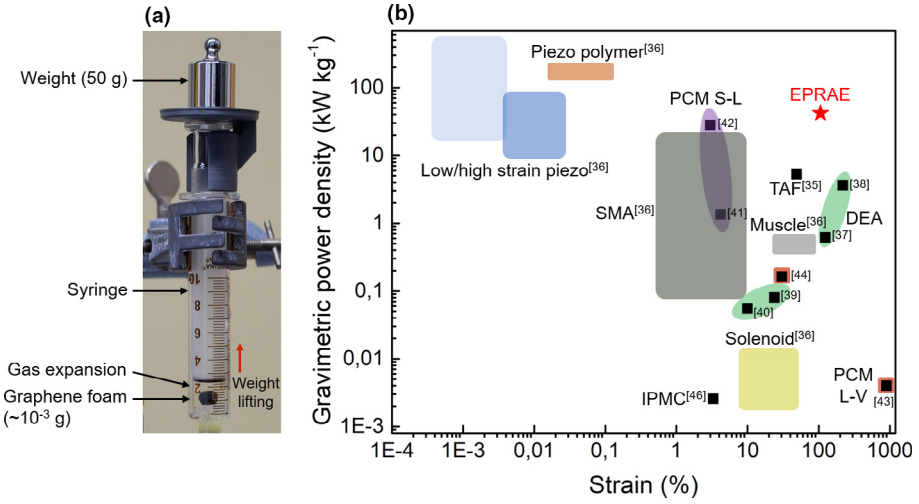

FIGURE 6

EPRAE-based actuator. (a) Photograph of EPRAE-based actuator consisting of a glass syringe with an integrated lightweight F-AM (~1.5 × 10–6 kg), employed for actuation of a weight (0.05 kg) within ~10 ms. The weight is lifted due to the gas volume expansion (106% with respect to the volume of the F-AM) caused by the EPRAE. The corresponding video is shown in the Supplementary Information (Video S4). (b) Gravimetric power density versus strain for various electrically powered actuator systems and the introduced EPRAE-based actuator. SMA: shape memory alloy, PCM: phase change material solid–liquid (S-L)/liquid–vapor (L-V), DEA: dielectric elastomer actuator, IPMC: ionic polymer metal composite, TAF: thermally activated fiber.

on top of a closed housing containing the F-AM could be repeatedly expanded at a high repetition rate by the EPRAE inside the chamber, demonstrating the potential for application in soft robotics.

EPRAE-based high-power actuator

Moreover, the EPRAE process enables actuator systems which show both high gravimetric power densities and large volume expansions. As demonstrated in Fig. 6a (details in Video S4), a F-AM with a weight of ~1.5 mg can rapidly and repeatedly actuate a weight of 65 g by ~1 mm in height (syringe diameter of ~1.5 cm) in ~0.01 s. It should be noted, that this experiment has been carried out using nitrogen as working gas in order to increase the possible temperature range. Even this unoptimized setup demonstrates that EPRAE-based actuators enable fast and large volumetric (~100% with respect to the volume of the F-AM) movements with output power densities (output power normalized to the weight of the transducer material) of ~40 kW kg^{-1}. Please note that the concept allows to increase systems inner energy by pre-compression and thus adopts easily to highest loads. As demonstrated in Video S4, even a weight of 2 kg can be lifted in 0.025 s by 2.2 mm, resulting in power densities >1000 kW kg^{-1} at 235% strain. In principle, even higher power densities can be reached, as the EPRAE actuator system is only limited by the stability of the F-AM, that can withstand even extreme heating rates of ~10^6 K s^{-1} (see Video S2) and the mechanical stability of the surrounding container. Generally, the F-AM did not show any mechanical degeneration during the weigh-lifting experiments, confirming the cycling stability demonstrated in Fig. 3. In comparison to other electrically driven actuator systems (Fig. 6b), the EPRAE process is capable of providing both a high strain and power density, thereby outperforming state-of-the-art actuator systems, e.g., based on shape memory alloys [36], piezo polymers [36], dielectric elastomers [37–40], and phase change materials [41–44]. In the future, soft robots that were limited by pneumatic tethers [45] or relied on irreversible combustion reactions [46], can be powered using the demonstrated EPRAE concept. Additionally, this concept could be further extended to fabricate electrically powered small-scale heat engines that can be operated at ambient conditions, as well as active and adaptive gas springs or dampers.

Conclusions

In summary, we introduced a new process that enables electrically powered repeatable air explosions utilizing graphene-based F-AMs. The concept is based on the framework structure of the graphene foams featuring large and open pores, which, in contrast to classical aerogels, allows for extremely fast (few ms) heating and cooling of macroscopic gas volumes. A broad range of sectors will benefit from the here introduced EPRAE concept. In microfluidics, the EPRAEs can be used for precise pumping, rapid switching of valves, rapid micro-actuators allowing for large and efficient volume changes (different to piezo-based systems), as well as micro-engines. Second, the EPRAE concept enables lightweight pneumatic systems on demand, useful for mobile applications, e.g. tactile displays and soft robotics, as well as pneumatic shock absorbers and car breaks. Additionally, basically all areas that require rapid activation of gases, such as in catalysis (e.g., by functionalizing the F-AMs with other nanomaterials), sensing, sorption and thermoacoustics (e.g., flat and omnidirectional loudspeakers) can benefit from the introduced concept. There are several other potential opportunities, including propulsion systems like thrusters used in satellites.

The EPRAE concept can be further extended by (I) the use of inert gases, such as nitrogen, which allow for even higher maximum temperatures (more than 3000 °C) and, thus, pressures/volume expansions that can be reached, and (II) increasing the compression ratio like in every combustion engine to obtain a multiple of pressure increase and volume expansion for the same

temperature difference. Thus, the EPRAE concept holds promise to reach Carnot efficiencies of more than 90%, which is unique for heat engines and close to that of conventional electrical engines.

Declaration of Competing Interest

The authors declare that they have no known competing financial interests or personal relationships that could have appeared to influence the work reported in this paper.

Acknowledgements

R.A., F.R., and F.S. acknowledge funding by the Deutsche Forschungsgemeinschaft (DFG) under contracts AD183/27-1, AD 183/18-1 and GRK 2154 and the Volkswagen Foundation in the scope of funding initiative "Experiment!" under contract A131464. This project has received funding from the European Union's Horizon 2020 Research and Innovation Programme under grant agreement No GrapheneCore2 785219, GrapheneCore3 881603, the FET Proactive ("Neurobres") grant No. 732344, the FET Open ("Boheme") grant No. 863179.

Author contributions

R.A., F.S., and F.R. developed the EPRAE concept. F.S., F.R., N.M.P, and R.A. designed the study. A.R.V., A.S.N., and M.R.L. prepared the nanomaterial dispersions (EG and GO) and the graphene aerogel. F.R., F.S., N.D., L.M.S., and A.R. fabricated the samples and carried out the Joule heating experiments. S.K., F.S. and F.R. constructed the experimental setup for the Joule heating characterization of the samples. S.K., F.S., A.R., and J.R. constructed the experimental setup for the gas flow and pressure measurements. F.S., F.R., J.R., S.K., L.M.S. and A.R. constructed the demonstration setups for the loudspeaker, micro-actuator, gas flowmeter, and thruster. F.S., F.R. N.D., and R.A. analyzed the data. F.R. performed the SEM and Raman characterization of the samples. D.M. and N.M.P. developed the mechanical modelling of the failure mechanisms, conducted the simulations of the failure mechanisms and analyzed the data. F.S., F.R., Y.K. M., R.A., A.S.N., M.R.L. X.F. and J.C., finalized the study and wrote the paper. All of the authors have contributed to the discussion of the results and reviewed the manuscript.

Data availability

The data that support the findings of this study are available from the corresponding authors upon request.

Competing interests

A patent application (DE102020110746.3) has been submitted based on these results.

Appendix A. Supplementary data

Supplementary data to this article can be found online at https://doi.org/10.1016/j.mattod.2021.03.010.

References

[1] R. Pape, K.R. Mniszewski, A. Longinow, Pract. Period. Struct. Des. Constr. 15 (2010) 135–140.
[2] K. Wüthrich, Chimia (aarau) 57 (2003) 757–765.
[3] Appendix A: Explosion and Fire Phenomena and Effects, in: Guidelines for Evaluating Process Plant Buildings for External Explosions and Fires, John Wiley & Sons, Ltd, 2010, pp. 131–148.
[4] K. Terao, Irreversible phenomena in ignitions, combustion and detonation waves, Springer, Berlin, London, 2007.
[5] M. Sakr, S. Liu, Renew. Sustain. Energy Rev. 39 (2014) 262–269.
[6] R. Menzel et al., Adv. Funct. Mater. 25 (2015) 28–35.
[7] D. Xia, H. Li, P. Huang, Nanoscale Adv. (2020).
[8] D. Xia et al., Chem. Commun. 56 (2020) 14393–14396.
[9] F. Yavari et al., Sci. Rep. 1 (2011) 166.
[10] Q. Zhang et al., J. Mater. Sci. 53 (2018) 528–537.
[11] W. Fei, J. Zhou, W. Guo, Small (Weinheim an der Bergstrasse, Germany) 11 (2015) 2252–2256.
[12] C.S. Kim et al., ACS Appl. Mater. Interfaces 8 (2016) 22295–22300.
[13] F. Giorgianni et al., Adv. Funct. Mater. 28 (2018) 1702652.
[14] A.K. Samantara, S. Ratha, S. Raj, Functionalized graphene nanocomposites in air filtration applications, in: A.E.K. Qaiss, M. Jawaid, R. Bouhfid (Eds.), Functionalized graphene nanocomposites and Their Derivatives: Synthesis, Processing and Applications, Elsevier Ltd, Amsterdam, Netherlands, 2019, pp. 65–89.
[15] Y. Xie et al., ACS Nano 13 (2019) 5385–5396.
[16] J. Ge et al., Nat. Nanotechnol. 12 (2017) 434–440.
[17] A.K. Geim, K.S. Novoselov, Nat. Mater. 6 (2007) 183–191.
[18] K. Shehzad et al., Three-dimensional macro-structures of two-dimensional nanomaterials, Chem. Soc. Rev. 45 (2016) 5541–5588.
[19] F. Rasch et al., ACS Appl. Mater. Interfaces 11 (2019) 44652–44663.
[20] R. Meija, et al., Nat Commun 8; 1–9.
[21] Engineering thermodynamics, McGraw Hill Education (India) Private Limited, Chennai, 2018.
[22] F. Schütt, et al., Nat. Commun. 8; 1–10.
[23] ZnO tetrapod materials for functional applications, Materials Today 21 (2018) 631–651.
[24] X. Zhang et al., J. Mater. Chem. 21 (2011) 6494–6497.
[25] K. Huang et al., Adv. Mater. Interfaces 5 (2018) 1701299.
[26] Thickness-dependent thermal resistance of a transparent glass heater with a single-walled carbon nanotube coating, Carbon 49 (2011) 1087–1093.
[27] M.A. Aegerter, N. Leventis (Eds.), Aerogels Handbook, Springer Science +Business Media LLC, New York, NY, 2011.
[28] Y. Xie et al., Carbon 98 (2016) 381–390.
[29] A. Passian et al., Ultramicroscopy 97 (2003) 401–406.
[30] S.G. Jennings, J. Aerosol Sci. 19 (1988) 159–166.
[31] N.K. Gupta, Y.B. Gianchandani, Appl. Phys. Lett. 93 (2008).
[32] M.N. Sweeting, T. Lawrence, J. Leduc, Low-cost orbit manoeuvres for minisatellites using novel resistojet thrusters, Proc. Inst. Mech. Eng., Part G: J. Aerospace Eng. 213 (1999) 223–231.
[33] M. Wehner et al., Nature 536 (2016) 451–455.
[34] J. Walker et al., Actuators 9 (2020) 3.
[35] C.S. Haines et al., Science 343 (2014) 868–872.
[36] J.E. Huber, N.A. Fleck, M.F. Ashby, Proc. R. Soc. Lond. A 453 (1997) 2185–2205.
[37] E. Acome et al., Science 359 (2018) 61–65.
[38] J.D.W. Madden et al., IEEE J. Ocean. Eng. 29 (2004) 706–728.
[39] M. Duduta, et al. Proc. Natl. Acad. Sci. U.S.A. 116 (2019) 2476–2481.
[40] H. Zhao et al., Adv. Funct. Mater. 28 (2018) 1804328.
[41] J.I. Lipton, Adv. Eng. Mater. 18 (2016) 1710–1715.
[42] M.D. Lima et al., Science 338 (2012) 928–932.
[43] A. Miriyev, K. Stack, H. Lipson, Nat. Commun. 8; 1–8.
[44] J.-H. Jeong et al., Nanoscale Adv. 1 (2019) 965–968.
[45] S.I. Rich, R.J. Wood, C. Majidi, Nat. Electron. 1 (2018) 102–112.
[46] N.W. Bartlett, Science 349 (2015) 161–165.

Supplementary Information for

Electrically powered repeatable air explosions using microtubular graphene assemblies

Fabian Schütt[1#], Florian Rasch[1#], Nipon Deka[1], Armin Reimers[1], Lena M. Saure[1], Sören Kaps[1], Jannik Rank[1], Jürgen Carstensen[1], Yogendra Kumar Mishra[2], Diego Misseroni[4], Adrian Romani Vázquez[3], Martin R. Lohe[3,5], Ali Shaygan Nia[3], Nicola M. Pugno[4,6], Xinliang Feng[3], Rainer Adelung[1]*

[1]*Functional Nanomaterials, Institute for Materials Science, Kiel University, Kaiser Str. 2, 24143 Kiel, Germany*

[2]*Mads Clausen Institute, NanoSYD, University of Southern Denmark, Alsion 2, 6400 Sønderborg, Dennmark*

[3]*Department of Chemistry and Food Chemistry, Center for Advancing Electronics Dresden (cfaed), Technische Universität Dresden, 01062 Dresden, Germany*

[4]*Laboratory of Bio-Inspired and Graphene Nanomechanics, Department of Civil, Environmental and Mechanical Engineering, University of Trento, via Mesiano 77, I-38123, Trento, Italy*

[5]*Sixonia Tech GmbH, Pestitzer Str. 16, 01187 Dresden, Germany*

[6]*School of Engineering and Materials Science, Queen Mary University of London, Mile End Road, London, E1 4NS, UK*

*Correspondence to: ra@tf.uni-kiel.de; fas@tf.uni-kiel.de
[#]Equal contribution

This PDF file includes:

Materials and Methods
Supplementary Text
- S1. Volumetric Heat Capacity Calculation
- S2. Specific Volumetric Surface Area Calculation
- S3. Exponential Fitting of Heating and Cooling Characteristics
- S4. Influence of Density of Framework-Aeromaterials (F-AMs) on the EPRAE Process
- S5. Thermo-Mechanical Failure Analysis of Tetrapods under Thermal Shock
- S6. Pump Efficiency Calculation

Figures S1 to S27
Tables S1 to S4
Captions for Movies S1 to S5

Other Supplementary Materials for this manuscript include the following:

Movies S1 to S5

Materials and Methods

Fabrication of Graphene and Graphene Oxide Dispersions

Graphene oxide (GO) was prepared according to previously reported procedures[1,2], followed by tip sonication in water to achieve a stable and homogeneous dispersion (2 mg mL^{-1}). Aqueous dispersions of electrochemically exfoliated graphene (EG, 2 mg mL^{-1}) were kindly provided by Sixonia Tech GmbH (Germany) and used without further modification.

Fabrication of Framework-Aeromaterials (F-AMs)

For the fabrication of the sacrificial templates, tetrapod-shaped zinc oxide (t-ZnO) microparticles were synthesized using the flame transport synthesis which has already been described in detail[3,4]. Briefly outlined, a powder mixture of polyvinyl butyral (PVB) and zinc (grain size 1-5 µm) with the mass ratio 2:1 was heated in a muffle furnace at 900 °C for 30 minutes. Burning of the sacrificial PVB created a flame which transported the Zn particles upwards, resulting in oxidation and formation of t-ZnO microparticles. Subsequently, the obtained t-ZnO powder was pressed into cylindrical tablets (6 mm in diameter and height) with 94% porosity. To obtain a mechanically stable network of interconnected t-ZnO particles, the templates were sintered at 1150 °C for 5 h.

The coating of the t-ZnO templates with the graphene-based nanomaterials was carried out using a previously reported wet-chemical infiltration method [5]. In brief, aqueous dispersions of GO and EG sheets were dribbled on the highly porous (94%) and hydrophilic t-ZnO templates, resulting in filling of the entire free volume of the template with dispersion. After drying of the templates (4h at 50 °C), the nanomaterial sheets were uniformly assembled on the t-ZnO surface forming a thin film coating on the entire template. The layer thickness is adjusted by increasing the number of infiltrations, resulting in a thin film thickness between 5 nm to 50 nm. The GO-coated t-ZnO templates were chemically reduced in diluted L-ascorbic acid (0.1 mg mL^{-1}) at 50 °C for 24 h.

In the last step, the sacrificial t-ZnO template was removed by wet-chemical etching in 1 M HCl for 24 h. To remove any remaining acid or contaminations the samples were several times washed with deionized water. Finally, the samples were transferred into pure ethanol and dried by critical point drying using an EMS 3000.

Aerogel Fabrication

Graphene oxide (Abalonyx AS, Norway) was dispersed in 50 ml of DI water at a concentration of 4 mg ml^{-1} using a 30-minute bath sonication treatment at room temperature. Subsequently, 0.6 g L^{-1} ascorbic acid was dissolved in the GO dispersion at room temperature and the mixture was separated into 5 portions á 10 ml in sealable glass vials. GO gels were formed by a thermal treatment of the sealed vials at 40°C for 24h without agitation. The resulting gel monoliths were removed from the vials and washed thoroughly overnight with water using a soxhlett extractor. Afterwards, the water was exchanged with absolute ethanol and subsequently dried using an EMS 3000 critical point dryer, yielding the freestanding graphene aerogels.

Density Characterization

The density ρ of the graphene-based F-AMs and aerogels was calculated by the following equation

$$\rho = \frac{m}{V} \qquad \text{(S1)}$$

where m is the mass and V the volume of the sample.

Electrical Characterization

The F-AMs or aerogels were mounted between two brass electrodes using conductive silver paste (ACHESON 1415). The electrical characterization was carried out using a Keithley 6400 sourcemeter in the four-wire sensing mode. Prior to the characterization, the samples were preconditioned by slow voltage ramping to achieve homogeneous Joule heating at ~300 °C in order to remove any residual moisture. To determine the resistance R of the F-AMs, I-V characteristics were recorded in the voltage range between -1 and 1 V. The resistance was taken as the slope of the linear I-V curve. The specific electrical conductivity σ was calculated using the following equation

$$\sigma = \frac{l}{R * A} \qquad \text{(S2)}$$

where l is the length of the sample and A is the cross-sectional area of the sample.

SEM Characterization

The samples were mounted on a sample holder with conductive carbon tape and SEM characterization was performed using a Zeiss Supra 55VP with the in-lens detector.

Raman Spectroscopy

Raman spectra were taken in ambient atmosphere using an alpha300 RA (WITec) microscope with a triple grating spectrometer (600 gr mm^{-1}) and a CCD detector. A green laser with an excitation wavelength of 532 nm was used. The spot size on the sample was ~1.41 µm. For the monitoring of the stability of Aero-EG during long-term EPRAE, the Raman spectra on three different spots of the sample were recorded at different time points during the long-term cycling. All spectra were baseline-corrected and averaged after acquisition.

Steady-State Joule-Heating and Cooling Characterization

The Joule-heating and cooling characteristics of the F-AMs were investigated by a high-speed pyrometer (Metis H318, SensorTherm GmbH, Germany) working in the temperature range between 120 °C and 550 °C with an acquisition time ~20µs. The F-AMs or aerogels were mounted between two brass electrodes using conductive silver paste (ACHESON 1415). The pyrometer was focused on the center of the sample. For all measurements the thermal emissivity was set to 0.99. The applied voltage, current, and temperature were measured as a function of time using a USB-2537 High-Speed DAQ Board (Measurement ComputingCorporation, USA) and a self-written LabView program. An EA-PS 2042-10B (EA Elektro-Automatik, Germany) was used as a power supply. All measurements were carried out by applying a defined constant voltage over a certain time period, e.g., 60 s, for all steady-state Joule-heating experiments. All measurements were carried out in ambient conditions.

Non-Steady-State Joule-Heating and Cooling Characteristics of EPRAE

The non-steady-state Joule-heating and cooling characteristics of the EPRAE process were measured using the same setup as described before. The applied voltage, power pulse width and repetition rate were set in the LabView program. All measurements were carried out in ambient conditions.

Rapid Volume Expansion Caused by EPRAE

The air volume expansion caused by individual EPRAEs was measured using the setup shown in Figure 4B. The housing (made out of PEEK) was designed in such a way that two brass electrodes

as well as two diaphragm check valves could be mounted. After mounting the F-AM between the two brass electrodes, the system was closed from the top using a transparent PMMA plate, resulting in a completely air-tight system that could be operated at isobaric conditions. By connecting a gas-flow transmitter (SFTE-1U-Q4-B-2.5K, Festo, Germany) to the check valve that opens when chamber pressure is increasing, the air flow caused by individual EPRAEs was measured over time using a USB-2537 High-Speed DAQ Board (Measurement ComputingCorporation, USA) and a self-written LabView program. After each power pulse (EPRAE), new air flowed into the chamber through the other check valve. EPRAEs were produced using the setup and LabView program described before. During data analysis, mathematical integration of the air flow yielded the change in volume.

Rapid Pressure Increase Caused by EPRAE

The increase in gas pressure caused by individual EPRAEs was measured using the same setup as for the measurement of the volume expansions, except that the outlet check valve and gas-flow transmitter were exchanged with a pressure sensor (MPX5100DP98ASA42797B, Mouser Electronics), resulting in an isochoric system. The pressure was recorded over time, together with the applied voltage, current, and temperature using a USB-2537 High-Speed DAQ Board (Measurement ComputingCorporation, USA) and a self-written LabView program.

Fabrication and Characterization of Micro-Pumps, Micro-Thrusters and Micro-Actuators Based on EPRAE

For the micro-pump and the micro-thruster, the same setup was used as described for the volume expansion measurements. For the micro-pump, a 30 cm long glass capillary (inner diameter of ~2 mm) was filled with a small amount of dyed water and connected to the outlet check valve of the chamber described before. The movement of the water caused by a series of EPRAEs was monitored using a video camera. Simultaneously, the applied voltage, temperature, current and air flow were measured with the same setup described before. In the case of the micro-thruster, a syringe needle (inner diameter of ~500 μm) was connected to the outlet check valve. The air thrust produced by a series of EPRAEs was monitored by recording the movement of a thin sheet of aluminum foil behind the needle with a video camera. Simultaneously, the applied voltage, temperature, and current were measured with the same setup described before. For the micro-

actuator, a thin latex membrane was mounted on a polymer capillary connected to the outlet port of the chamber and sealed using a seal ring. The deformation of the latex membrane caused by a series of EPRAEs was recorded using a video camera.

Fabrication of In-Ear Thermophone

The in-ear thermophone was fabricated by removing the electrical components from the housing of a commercially available in-ear loudspeaker. A cylindrical F-AM was connected to two thin cooper plates by means of a 3D printed mount. The cooper plates were connected to the input of the in-ear headphone. For sound generation a tablet and a frequency generator app were used.

Supplementary Figures, Tables and Text

Voltage and Current Characteristics during EPRAE

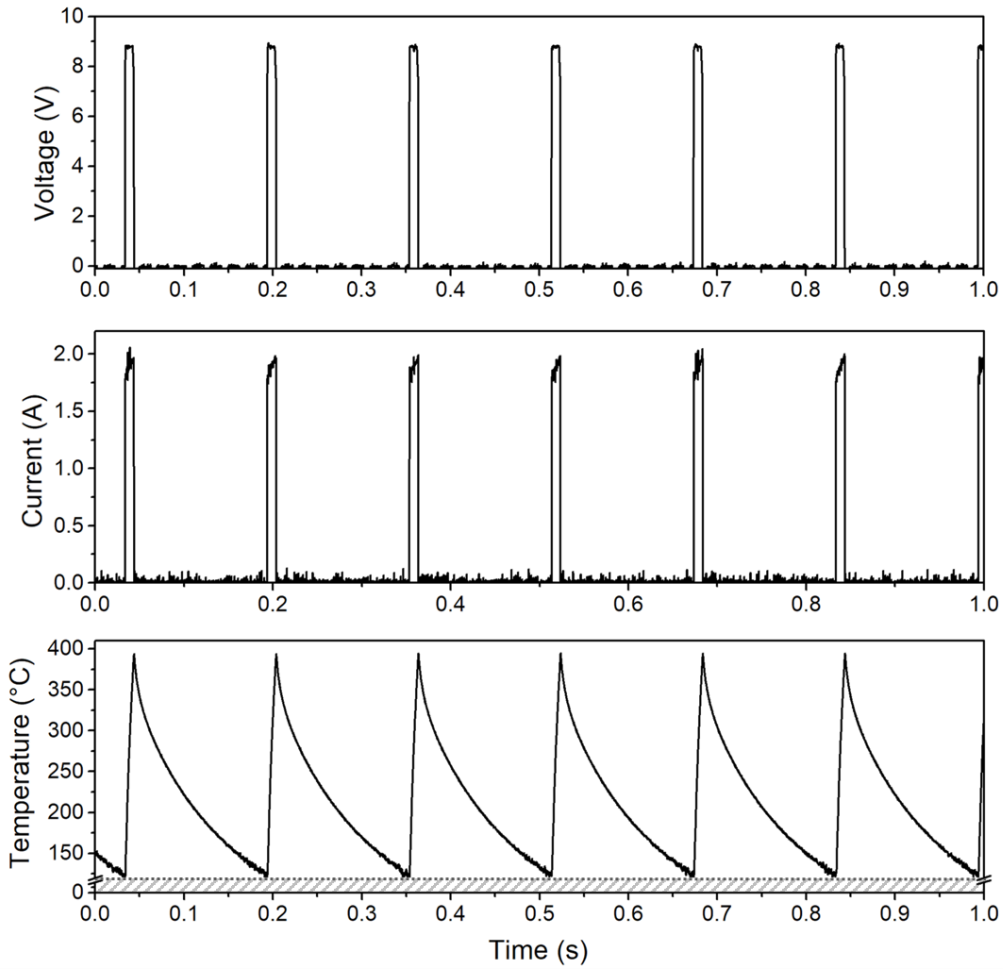

Figure S1. Voltage-, current-, and corresponding temperature-time profiles for a typical EPRAE process, induced by 10 ms power pulses (peak power ~18 W) at a repetition rate of ~6.7 Hz. Peak voltages and currents of ~9 V and ~2.1 A were reached, respectively.

F-AM Fabrication and Characterization

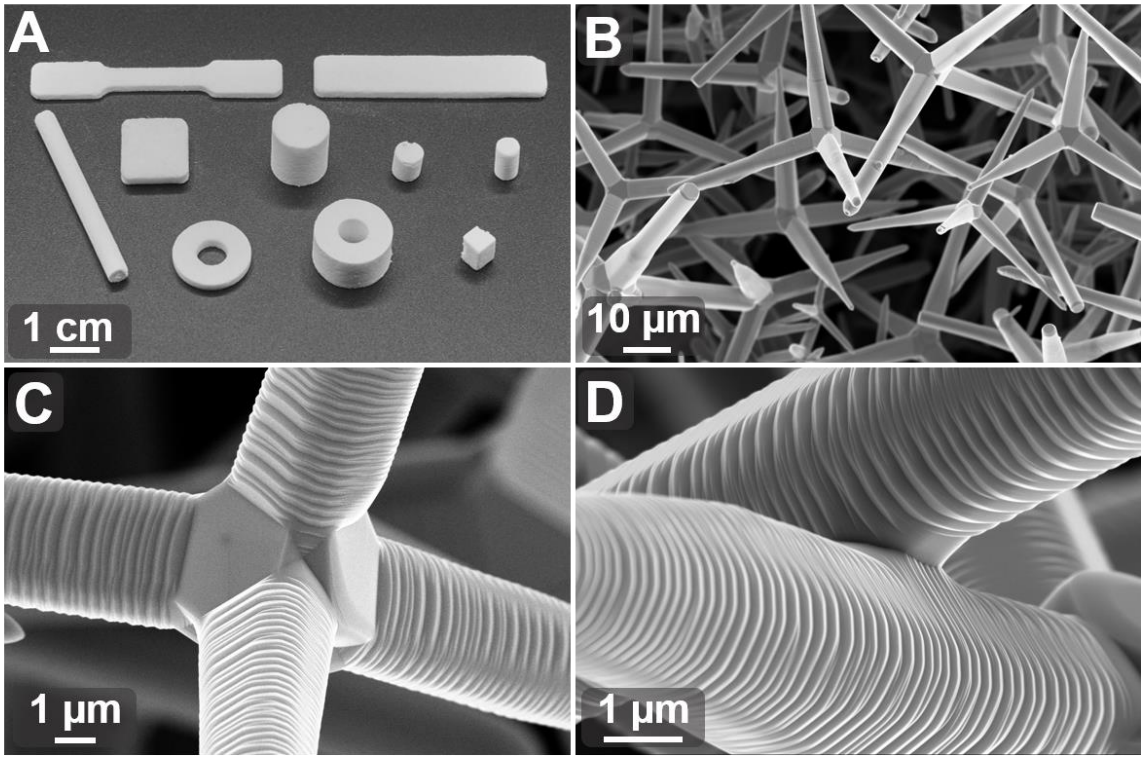

Figure S2. Sacrificial t-ZnO templates. (A) Photograph of several t-ZnO templates with various different geometries. (**B**)-(**D**) SEM images of a t-ZnO template with increasing magnification, revealing the framework-like structure consisting of interconnected ZnO microrods.

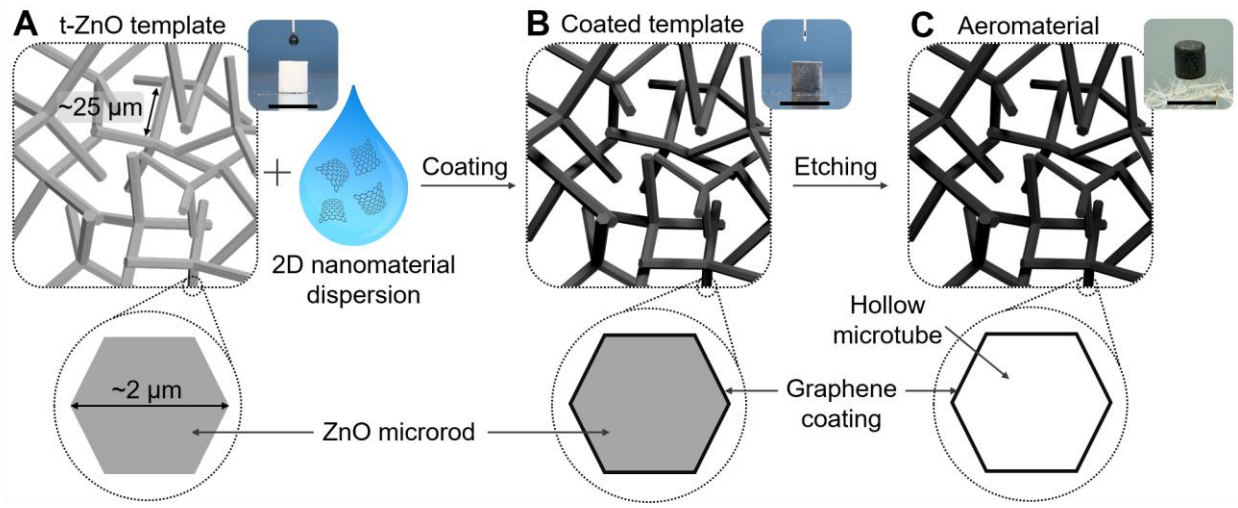

Figure S3. F-AM fabrication. Schematic presentation of the F-AM fabrication steps: (**A**) Wet-chemical infiltration of the porous (94%) t-ZnO template with an aqueous dispersion of 2D nanomaterials (in this work: electrochemically exfoliated graphene and graphene oxide). (**B**) After drying of the template, the 2D nanomaterial sheets assembled on the template surface, resulting in a uniform, nanoscopic coating on the interconnected ZnO microrods. (**C**) After wet-chemical removal of the t-ZnO template in 1 M HCl and subsequent criticial point drying, the final F-AM was composed of interconnected hollow (graphene) microtubes. Scale bar in photographs: 1 cm.

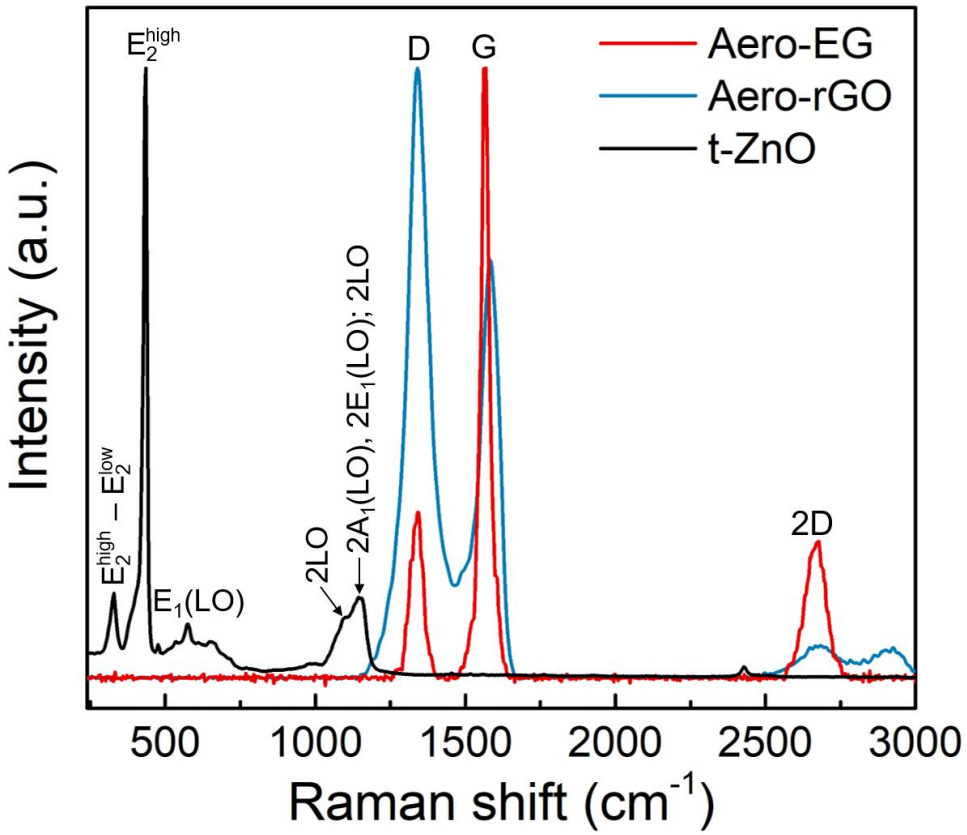

Figure S4. Raman microscopy. Raman spectra of the employed t-ZnO template and the F-AMs (Aero-EG, Aero-rGO).

S1. Volumetric Heat Capacity Calculation

The determination of the volumetric heat capacity of extremely porous and low-density materials, such as the F-AMs presented in or work, is not easily feasible with available standard measurement techniques such as the laser flash method. To obtain reasonable values we carried out some rough estimate based on our measurement data given in Figure 2I.

The volumetric heat capacity *s* of a material is defined as

$$s = c * \rho \qquad \text{(S3)}$$

where c is the specific heat capacity and ρ is the density of the material, respectively.

While we know the densities ρ of the AMs, we have no measure of their specific heat capacity *c*. As a rough estimate *c* could be approximated by the specific heat capacity of graphite, having a value of 0.72 J g^{-1} K^{-1}.

However, based on Joule's first law of heating, which states that an electric current in an electrical conductor produces the thermal energy *Q* generated by a continuous conversion of the supplied electrical energy *E*

$$Q = E \qquad \text{(S4)}$$

with *Q* and *E* being defined as

$$Q = \frac{c}{m*\Delta T} \qquad \text{(S5)}$$

$$E = P * t = \frac{U^2*t}{R} \qquad \text{(S6)}$$

with *m* being the mass, ΔT being the difference between end and start temperature, *P* being the supplied electrical power over the duration *t*, *U* being the applied voltage and *R* being the resistance, we can calculate the specific heat capacity *c* of the AMs by:

$$c = \frac{U^2*t}{R*dT*m} \qquad \text{(S7)}$$

The data used for the calculation is extracted from the measurement shown in Figure 2I, resulting in a value of 0.367 J g^{-1} K^{-1}, which is reasonably close to that of graphite.

Therefore, an AM with a density ρ of ~ 8 mg cm^{-3} can be estimated to have a volumetric heat capacity in the order of 2 to 6 kJ m^{-3} K^{-1}, which is on the same order of magnitude compared to that of gases. For instance, air at 0°C has a specific volumetric heat capacity of ~1.3 kJ m^{-3} K^{-1}.

S2. Specific Volumetric Surface Area Calculation

The specific volumetric surface area (VSA) of the F-AMs (AMs) plays a crucial role in the Joule heating characteristics. Nevertheless, for lightweight macroscopic framework structures having a high free volume (>90%), it is difficult to obtain the specific gravimetric surface area (GSA) by standard techniques, such as BET, due to the fact that the overall amount of material per volume is rather low. However, since the fabrication of the F-AMs is based on a templating process, the specific gravimetric and volumetric surface area can be estimated using the following calculation. Similar calculations have already been applied for graphene foams grown by nickel-foam assisted CVD.[6]

The t-ZnO template density (ρ_{Template}) for all the F-AMs used in our work was ~0.3 g cm^{-3} (porosity ~94%). Furthermore, for the single microrod building blocks of the template, we assume a cylindrical geometry with a constant microrod length (l_{mr}) and diameter (d_{mr}) of 25 µm and 2 µm, respectively.

Based on these boundary conditions and taking into account a density of 5.61 g cm^{-3} for ZnO (ρ_{ZnO}), the surface area of each microrod (without the end faces) A_{mr}, the number of microrods per unit volume (n_{mr}) and, thus, the specific volumetric surface area of the template can be calculated:

$$A_{mr} = d_{mr} * \pi * l_{mr} \cong 1.57^{-10}\ m^2 \qquad \text{(S8)}$$

$$n_{mr} = \frac{\rho_{Template}}{\pi * \left(\frac{d_{mr}}{2}\right)^2 * l_{mr} * \rho_{ZnO}} \cong 6.8 * 10^8\ \frac{1}{cm^3} \qquad \text{(S9)}$$

$$VSA_{Template} = n_{mr} * A_{mr} \cong 0.107\ \frac{m^2}{cm^3} \qquad \text{(S10)}$$

Taking into account that the final F-AM structure consists of hollow microtubes instead of microrods, the estimated volumetric surface area of the AMs will be ~2 times that of the template.

$$VSA_{AM} = 2 * VSA_{Template} \cong 0.214\ \frac{m^2}{cm^3} \qquad \text{(S11)}$$

However, since the F-AMs consist of several stacked graphene sheets, the above estimated surface area can be assumed as a lower limit.

Steady-State Joule-Heating Characteristics

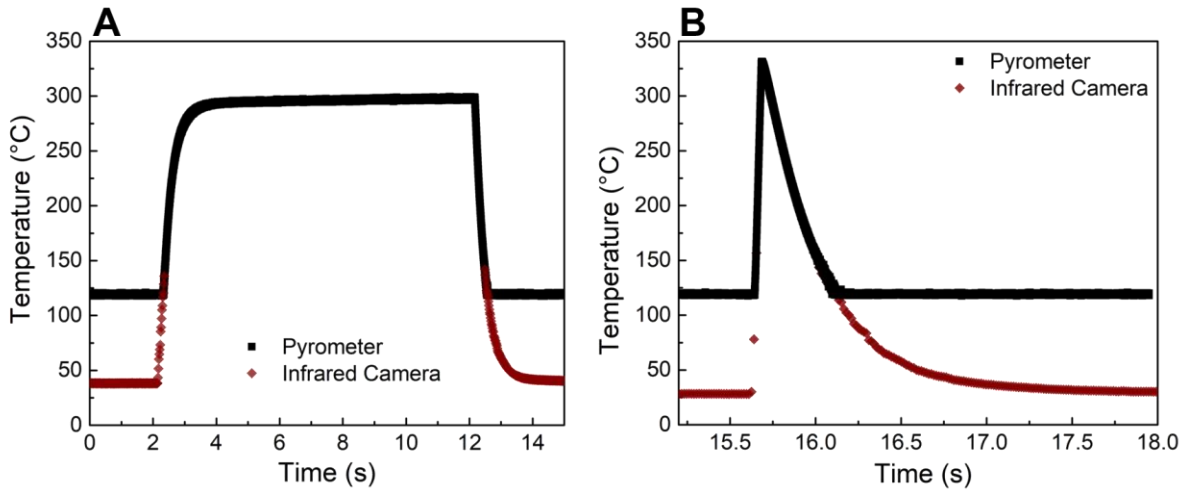

Figure S5. Joule-heating characteristics of F-AM in complete temperature range. Temperature-time profiles of Aero-rGO for (**A**) steady-state Joule heating and cooling and (**B**) a rapid Joule heating and cooling cycle, measured with a high-speed pyrometer and an infrared camera to cover the entire temperature range.

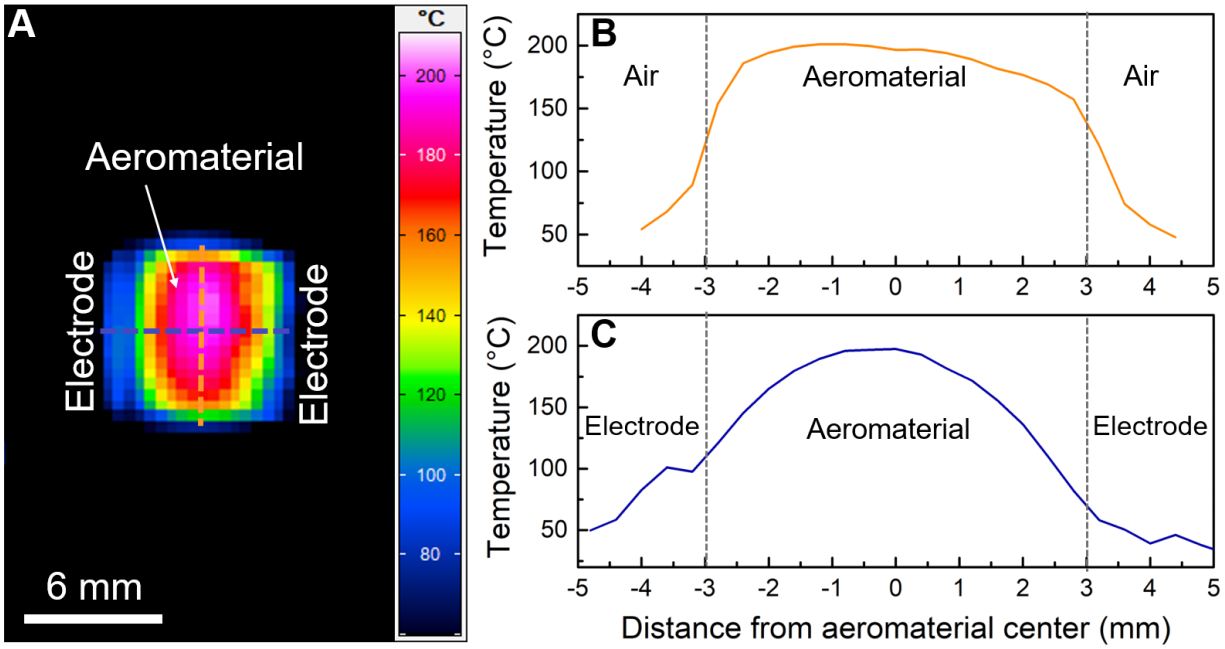

Figure S6. IR imaging of F-AM during steady-state Joule heating. (**A**) Thermal IR image of Aero-rGO during steady-state Joule heating. The marked dotted orange and blue lines correspond to (**B**) the transverse temperature profile and (**C**) the axial temperature profile, respectively.

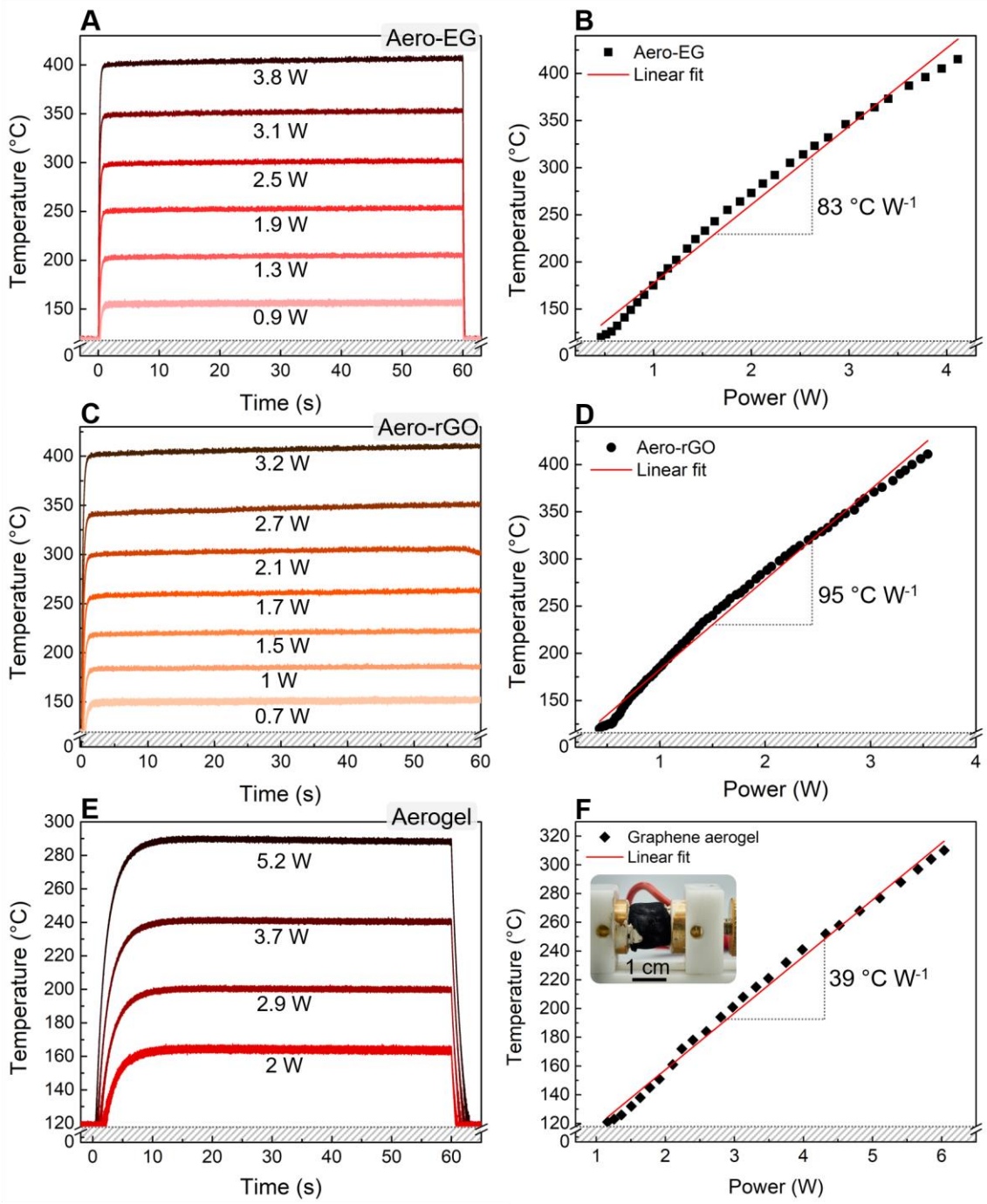

Figure S7. Joule-heating characteristics. Steady-state Joule-heating and cooling characteristics at different applied powers and the corresponding temperature-power relationship for (**A**)-(**B**) Aero-EG (~8 mg cm^{-3}), (**C**)-(**D**) Aero-rGO (~7 mg cm^{-3}), and (**E**)-(**F**) the graphene aerogel (~22 mg cm^{-3}).

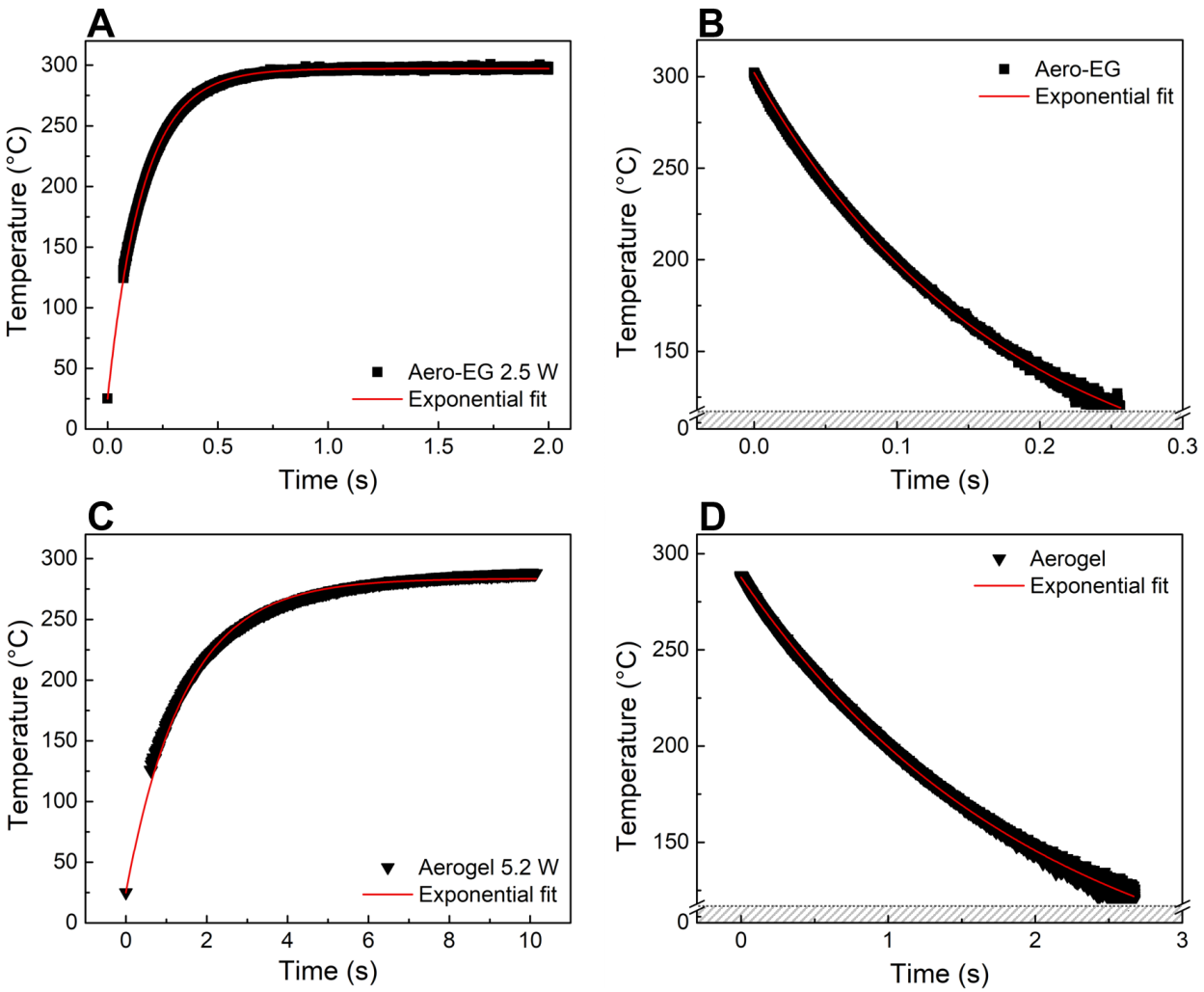

Figure S8. Exponential fitting of heating and cooling characteristics. Exemplarily, the exponential fits of the steady-state heating and cooling curves for 300 °C are presented for (**A**)-(**B**) Aero-EG and (**C**)-(**D**) the graphene aerogel, respectively. The mathematical model used for the fits is described in the Supplementary Text.

S3. Exponential Fitting of Heating and Cooling Characteristics

To obtain the heating and cooling time constants from the steady-state Joule-heating and cooling profiles (Figure 2E and Figure S6), the corresponding heating and cooling curves were fitted with the following exponential function

$$y = y_0 + A\left(1 - exp\left(\frac{-t}{\tau}\right)\right) \qquad \text{(S12)}$$

where y_0 is the starting temperature (25 °C for heating curve, T_{max}~400 °C for cooling curve), A is a constant, t is the time, and τ is the time constant (τ_H: heating time constant, τ_C: cooling time constant). The exponential fits for the heating and cooling curves of Aero-EG and the graphene aerogel are exemplarily shown in Figure S7 for one steady-state temperature (~300 °C). After determining the time constants for various steady-state temperatures, the heating and cooling time constants were plotted versus the corresponding temperature, as depicted in Figure 2F of the main manuscript.

Structural Comparison of Framework-F-AM and Aerogel

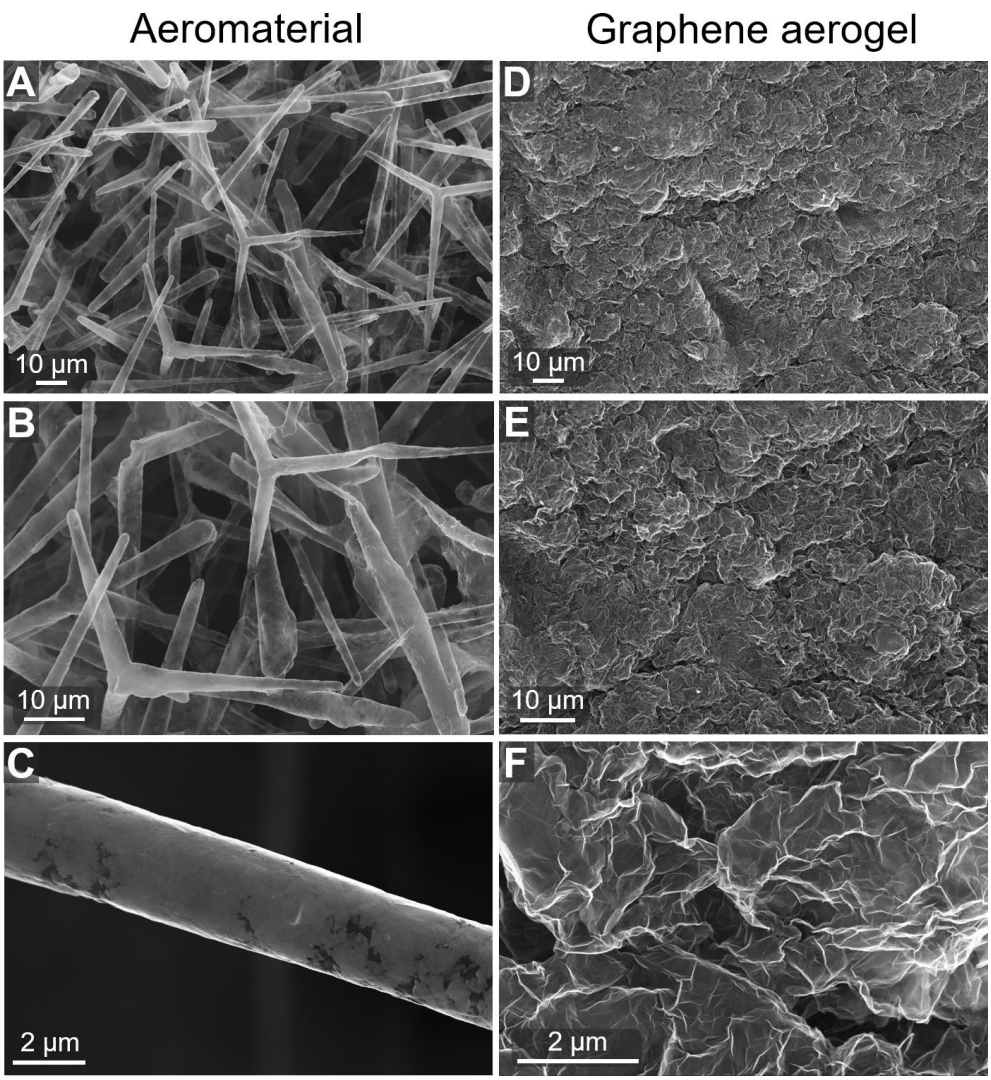

Figure S9. Structural comparison of a F-AM and aerogel. SEM images of (**A**)-(**C**) Aero-EG (representative for the F-AMs) and (**D**)-(**F**) the graphene aerogel with similar magnifications, revealing significant differences in the structure and pore sizes of the materials.

Mean Heating and Cooling Rates

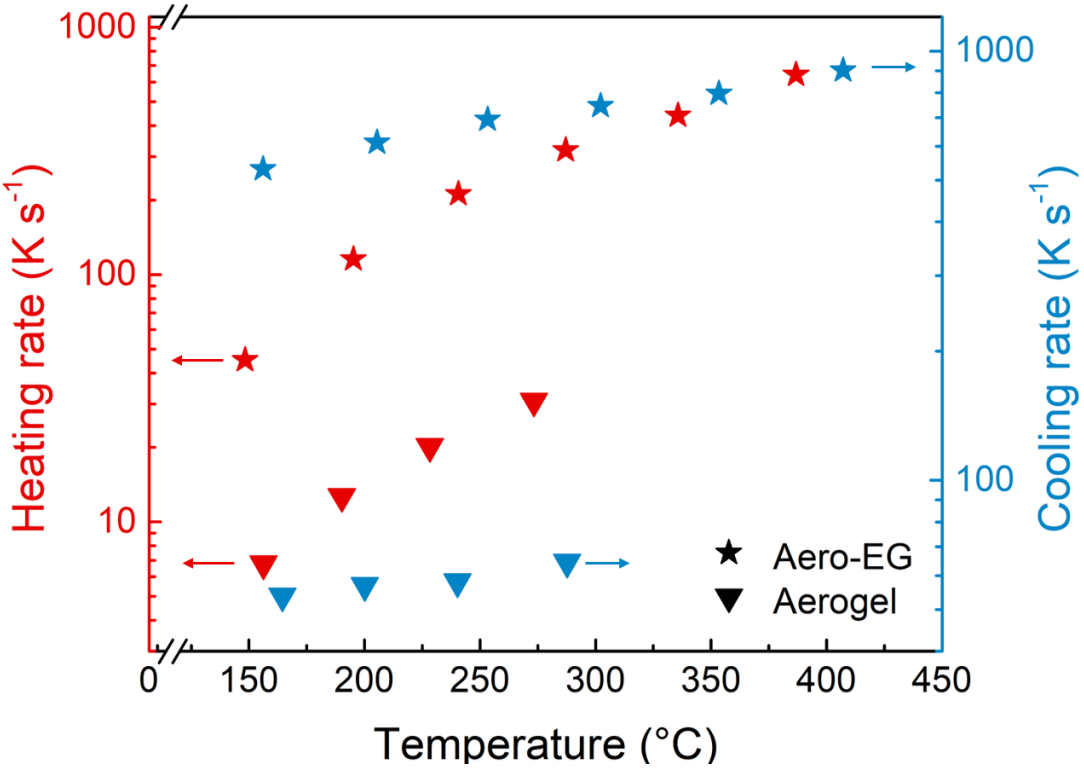

Figure S10. Heating and cooling rates. Mean heating and cooling rates for several steady-state temperatures, measured for Aero-EG and the graphene aerogel. For the calculation of the mean heating rates, the heating temperature was defined to be 95% of the maximum temperature.

Non-Steady-State Joule-Heating Characteristics

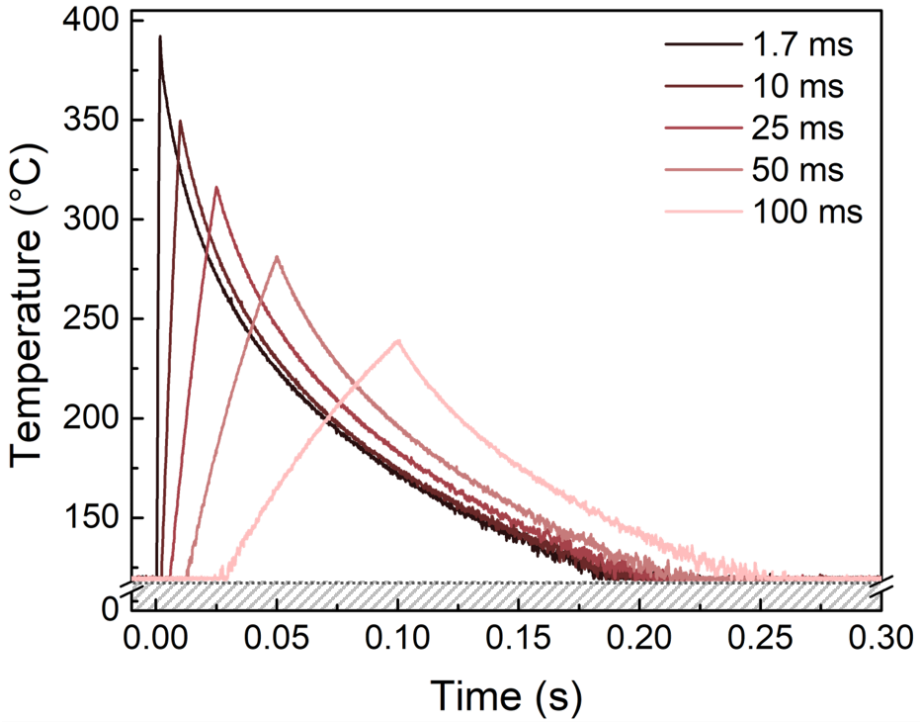

Figure S11. Tunable Joule-heating characteristics. Temperature-time profiles for rapid Joule-heating pulses of Aero-EG at constant energy input and increasing pulse duration.

S4. Influence of Density of Framework-Aeromaterials (F-AMs) on the EPRAE Process

The density (ρ) of the F-AMs is directly related to the amount of graphene or graphene oxide that is used to coat the ceramic template materials. [5]

The density of the F-AMs affects the mechanical, electrical and thermal properties of the F-AMs. As shown in Figure 2C of the main manuscript, the electrical conductivity as well as the volumetric heat capacity increase with increasing density of the F-AMs. The influence of the density on the mechanical properties of the F-AMs was previously reported by Rasch et al., demonstrating enhanced mechanical stability with increasing density.[5]

With respect to the introduced EPRAE process, there are two main competing mechanisms that determine the optimal density of the F-AMs. The heating and cooling characteristics of the F-AMs are mainly determined by their volumetric heat capacity. The lower the volumetric heat capacity, the faster the materials can be heated and cooled, meaning that a low density is highly desired. However, the rapid volume expansions and temperature gradients caused by the EPRAE process require the F-AMs to withstand high forces produced by the heated gas that is rapidly pushed out of the F-AMs. Therefore, a high F-AM density is beneficial to ensure mechanical stability of the EPRAE system.

From our experiments with different F-AM densities, we deduced that the optimal density is in the range of 4 to 8 mg cm^{-3}, providing volumetric heat capacities in the range of that of gases, while being mechanically stable enough to withstand even extremely rapid (~1 ms) gas expansions. As can be seen in Video S2, an extremely fast heating (50 µs) of the F-AMs to ~220 °C (peak power of 576 W) results in disintegration of the F-AM, with whole macroscopic parts of the F-AM being pushed out from the structure by the extremely rapid volume expansion of the gas.

Long-Term Stability of Electrically Powered Repeatable Air Explosions (EPRAE)

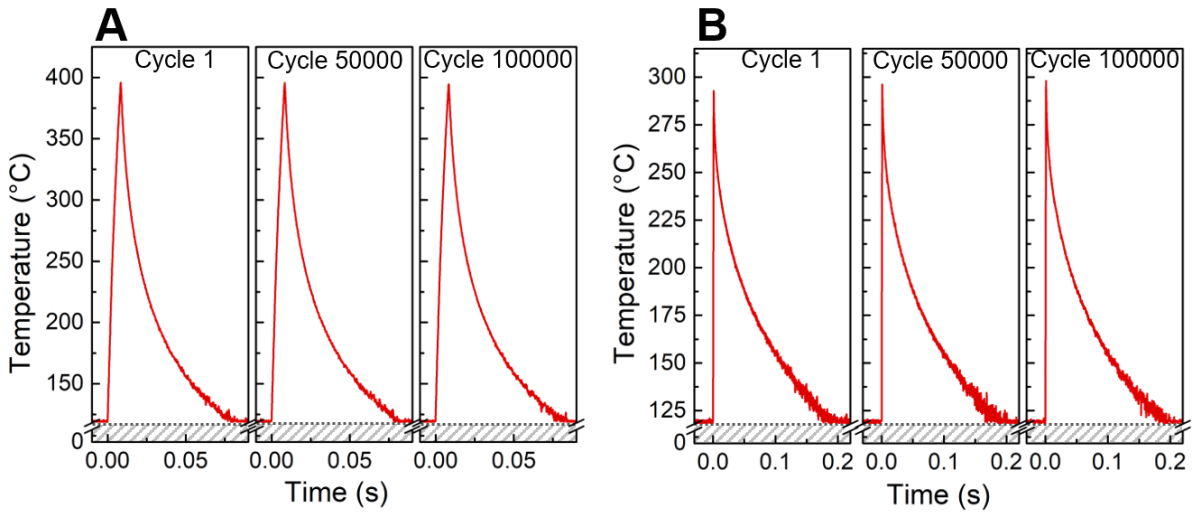

Figure S12. Long-term pulsed heating of F-AMs. Temperature-time profiles for (**A**) Aero-rGO and (**B**) Aero-EG during repetitive Joule-heating and cooling cycles, shown for the cycle 1, 50000, and 100000. Please note that the Aero-rGO sample has been pulsed for additional 100000 cycles (Figure 3A, main manuscript), yielding in total 200000 stable cycles for more than 2 days.

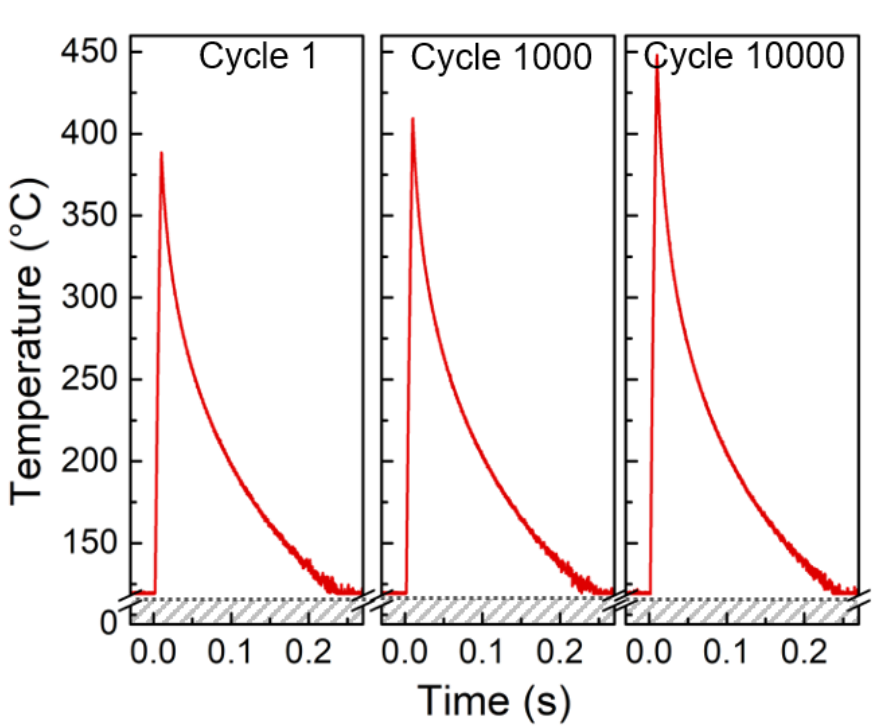

Figure S13. Long-term pulsed heating of F-AMs. Temperature-time profiles for Aero-EG during repetitive Joule-heating and cooling cycles, shown for the cycle 1, 1000, and 10000. The increasing maximum temperature (with progressing Joule-heating cycles) indicates partial mechanical failure of the F-AM. In particular, partial fractures within the sample lead to less uniform Joule heating with locally increased current densities, resulting in local temperature increase and, ultimately, mechanical failure.

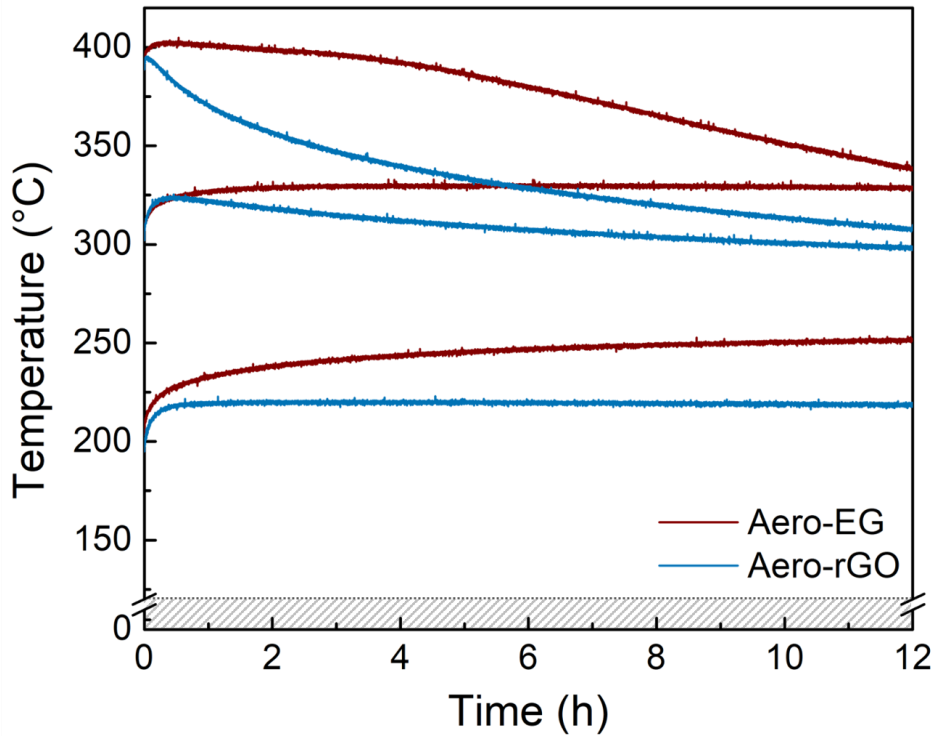

Figure S14. Long-term Joule heating of F-AMs. Temperature-time profiles of Aero-EG and Aero-rGO during long-term steady-state Joule heating for three different starting temperatures measured at a fixed voltage.

For a starting temperature of ~400°C the maximum measured temperature of Aero-EG and Aero-rGO is strongly decreasing over time, indicating a strong oxidation of both EG and rGO over time, resulting in a decrease in electrical conductivity and, thus, power. At starting temperatures of ~300 °C and 200 °C, the maximum temperature of Aero-EG increases over time. At these temperatures, no oxidation of the EG takes place, but residual moisture is removed between the individual EG sheets[7], resulting in an increase in electrical conductivity and, thus, supplied power. The same effect can be observed in the case of Aero-rGO at both 200 °C and 300 °C starting temperature. However, at 300 °C, the maximum temperature of Aero-rGO starts to slowly decline after 2h of measurement, indicating that at these temperature rGO already starts to oxidize.

Structural Investigation of F-AMs after EPRAE

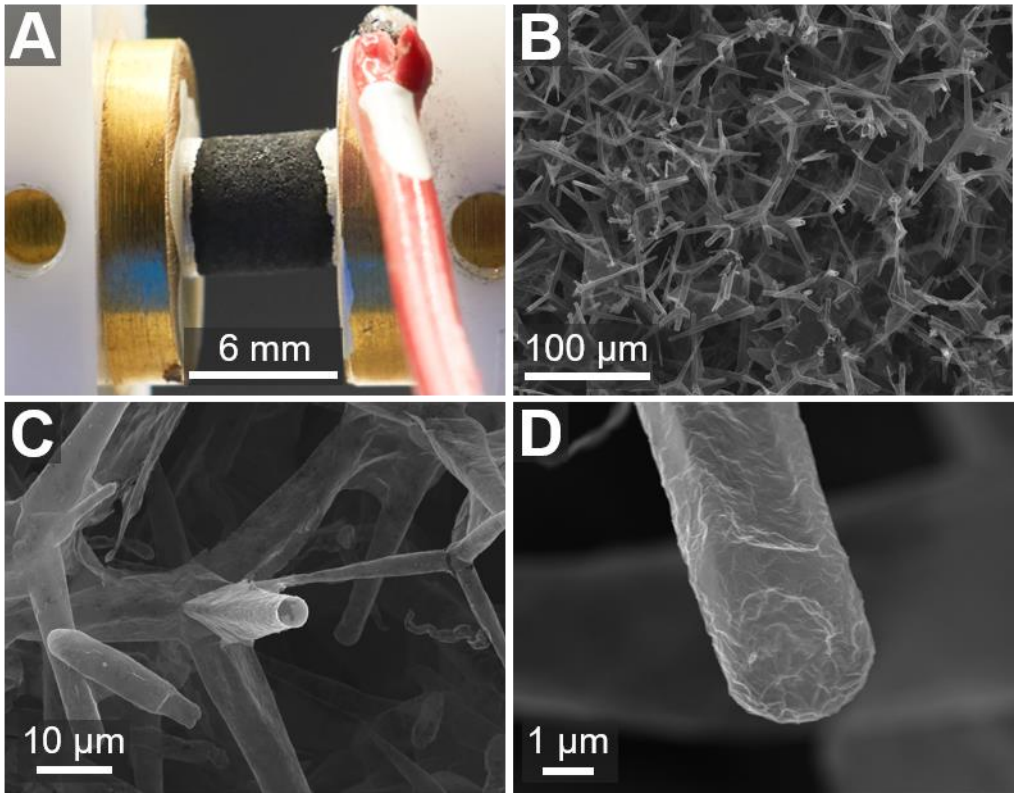

Figure S15. Structural stability of F-AMs after long-term cycling. (**A**) Photograph and (**B**)-(**D**) SEM images of Aero-EG after 10000 EPRAE cycles, revealing the macroscopic and microscopic structural integrity.

In situ Raman spectroscopy

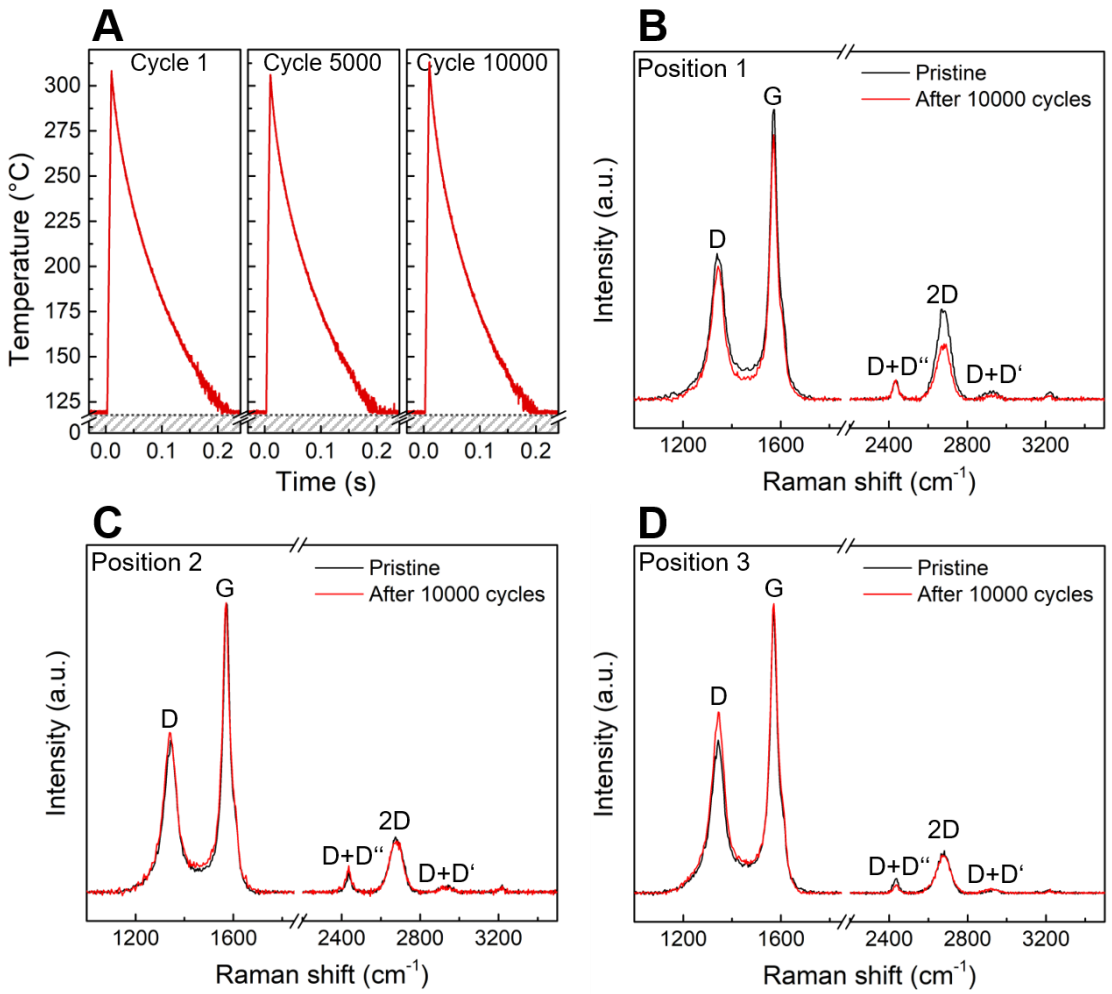

Figure S16. *In situ* Raman spectroscopy of Aero-EG. (**A**) Temperature-time profiles of Aero-EG during repetitive Joule heating and cooling, showing cycle 1, 5000, and 10000, respectively. (**B**)-(**D**) The corresponding Raman spectra of the same Aero-EG sample are shown before and after the long-term cycling at three different sample positions.

The Raman spectra reveal 5 different bands for Aero-EG (see labels), which are characteristic for graphene[8]. The most prominent peaks (arising from first-order phonons) are the D band (~1340 cm^{-1}), corresponding to the breathing mode of aromatic six-atom rings and only activated by defects, and the G band (~1580 cm^{-1}), which is caused by in-plane bond-stretching of pairs of carbon sp^2 atoms. Additionally, the second-order phonons are the D+D´´ band (~2435 cm^{-1}), originating from a combination of a D phonon and a phonon from the LA branch (D´´), the 2D band (~2680 cm^{-1}), corresponding to the D-peak overtone, and the D+D´ band (~2950 cm^{-1}), resulting from a combination of one intravalley and one intervalley phonon scattering process

under the presence of defects.[8–11] The intensity ratio of the D and G band, $I(D)/I(G)$, is a commonly accepted tool to probe the defect density of graphene. The relatively low $I(D)/I(G)$ ratio of the investigated Aero-EG sample (Fig. S12B-D) indicates the occurrence of high-quality graphene flakes and confirms the Raman results of recent studies using the same EG dispersion.[5,12] The presence of the D band in the spectra might be related to a small fraction of oxygen-containing functional groups, resulting from the fabrication process[12], and due to the fact that the laser spot size (~1.4 µm) is larger than the lateral size of some of the EG flakes and, thus, leads to probing of edge "defects". After 10000 EPRAE cycles (temperature-time profile of one cycle in Figure S14a), the $I(D)/I(G)$ ratio increased slightly at position 1 and 3 of the Aero-EG sample, indicating a small increase in the defect density which might have been caused by partial oxidation of the EG flakes during the fast (10 ms) heating pulses to 300 °C. The 3 second-order peaks at higher wavenumbers do not reveal a significant change after 10000 EPRAE cycles, except a decreased intensity of the 2D band at position 1. In summary, however, the Raman spectra show only minor changes after long-term EPRAE, demonstrating the good chemical stability of Aero-EG during the process.

S5. Thermo-Mechanical Failure Analysis of Tetrapods under Thermal Shock

S5.1. Thermo-mechanical models for the tetrapod failure

This section is devoted to discussing the mechanical mechanisms that could lead to the breaking of the tetrapod subject to an instantaneous thermal shock. The tetrapods experience a severe temperature gradient; the temperature within the cavity (and so the temperature of the inner surface of the tube, T_i) increases from an initial value of 293.15 K to a final value of 673.15 K in about 1 ms, corresponding to a thermal jump $\Delta T = T_e - T_i = -380$ K. In the analysis, we assume that the temperature of the outer surface of the tube, T_e, remains the same as the initial value of 293.15 K. Such assumption is justified observing that, since the temperature increase is very sharp, the cavity is subject to an "almost" adiabatic process (no heat exchange with the environment) while the outer surface, being in an opened ambient, can exchange the heat with the air and, therefore, keeps a lower temperature. In particular, three main mechanical models are thoroughly discussed and analysed. All the approaches yield the generation of the hoop and longitudinal stresses in the thin-walled hollow tetrapod. In the calculation we assume i) the material mechanical properties E=1 TPa (Young's modulus)[13], υ=0.43 (Poisson's ratio)[13], ϱ=2272 kg m^{-3} (density)[14], α_T =-3.75x10^{-6} K^{-1} (coefficient of thermal expansion)[14], κ=2200 W m^{-1} K^{-1} (thermal conductivity)[15], c=700 J kg^{-1} K^{-1} (specific heat)[16] and ii) for the geometry of the tetrapod an average wall thickness t = 10 nm, a tube diameter d=2 μm (outer radius r_e=1.005 μm, inner radius r_i =0.995 μm) and a tube length L=25 μm. The geometrical parameters needed to perform the analytical calculations and the numerical simulations are highlighted in Figure S15.

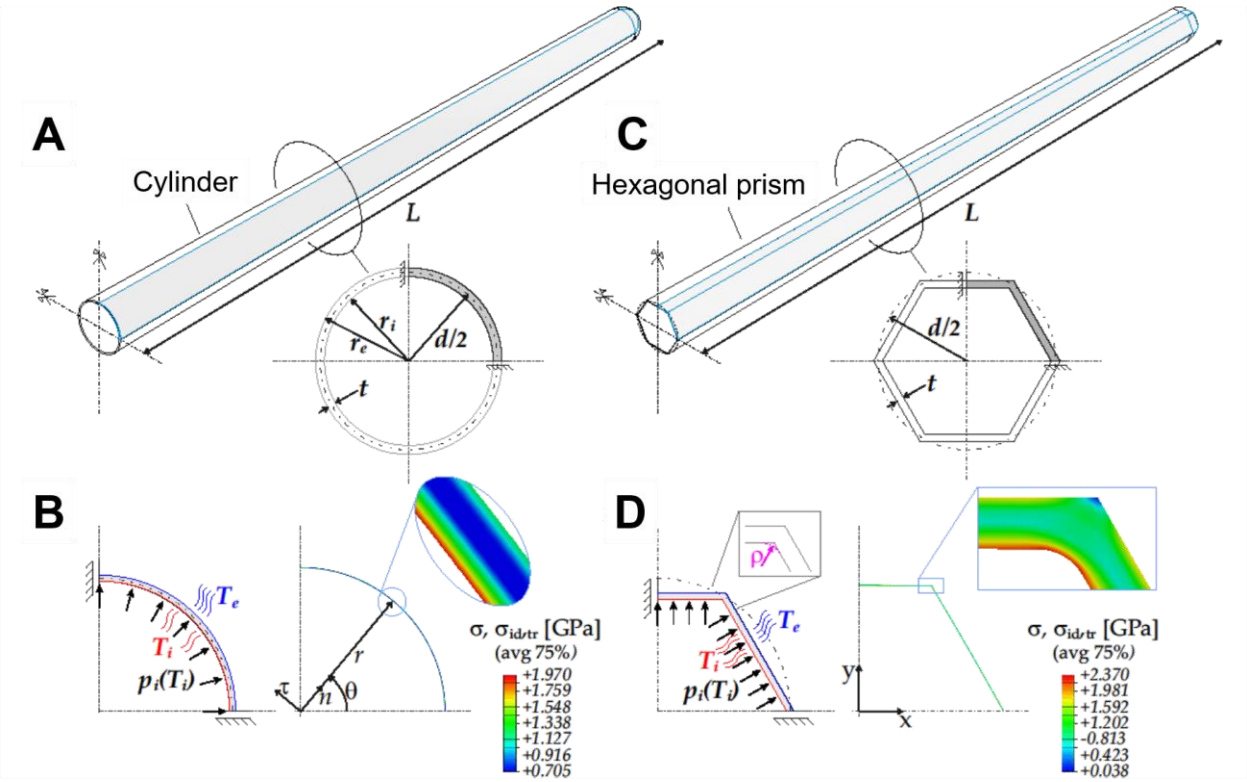

Figure S17. Geometrical approximation of the tetrapod shape and numerical results. (**A**) The tetrapod is approximated with a cylindrical tube or (**B**) with a truncated hexagonal hollow prism. (**C**)-(**D**) Numerical results from a thermo-mechanical analysis of the tetrapod subject to the internal pressure p_i=131.344 kPa and the temperature jump ΔT=380 K for (**C**) a cylindrical and (**D**) a hexagonal geometry. The numerical simulations were performed assuming the geometrical parameters t=10 nm, d=2 μm (outer radius r_e=1.005 μm, inner radius r_i=0.995 μm), and ϱ=10 nm.

In Table S1, a comprehensive summary of the failure stresses, predicted from the theory and the numerical simulations, is reported. The simulations were performed approximating the tetrapod tube with a cylindrical geometry or a truncated hexagonal hollow prism, as shown in Figure S15, assuming the geometrical parameters t=10 nm, d=2 μm (outer radius r_e=1.005 μm, inner radius r_i=0.995 μm), inner fillet radius ϱ=10 nm. It is worth mentioning that, considering the hexagonal prism geometry, the maximum stress in the case (A) is susceptible to the junction (inner) fillet radius ϱ, highlighted in Figure S15, if $\varrho \to 0$, a singularity arises leading to a considerable intensification of stress.

Table S1. Comparison between the maximum stress σ_t predicted from the theory and those predicted from the numerical simulations for different failure mechanisms: (A) air expansion, (B) thermal stress, (AB) air expansion + thermal stress, (C) air thrust. The analytical calculations were conducted approximating the tetrapod tube with cylindrical geometry. The numerical simulations were carried out approximating the tetrapod tube with a cylindrical geometry or with a truncated hexagonal hollow prism, both having t=10 nm and d=2 μm (outer radius r_e=1.005 μm, inner radius r_i=0.995 μm). For the simulations, the Tresca maximal stress ($\sigma_{id,tr}$) is reported, as well. **All the results reported in the columns "hexagonal prism" are obtained assuming an inner fillet radius ϱ=10 nm. *For the hexagonal shape, the maximum stress (case (A)) is susceptible to the junction (inner) fillet radius ϱ, highlighted in Figure S15d.

Failure mechanism	Theory cylinder	Abaqus simulations			
		Cylinder		Hexagonal prism**	
	σ_t [MPa]	σ_t [MPa]	$\sigma_{id,tr}$ [MPa]	σ_t [MPa]	$\sigma_{id,tr}$ [MPa]
(A)	13.13	13.20	13.33	747.9*	753.0*
(B)	1254.2	1254	1964	1449	2048
(AB)	1267.3	1267	1970	2197	2370
(C)	0.31	-	-	-	-

Analyzing the numerical (and theoretical) results, we can conclude that the tetrapod breaks, most likely, according to the mechanism (AB), combination of the mechanism (A) and (B), with the latter being the main responsible. We emphasize that the predicted stress is independent from the Young's modulus for the mechanism (A) and linearly dependent for the mechanism (B), see Equations S18, S19, and S24, respectively. Combining experimental observations and numerical results we can conclude that the Tresca maximal strength of the tetrapod is less than 2.4 GPa.

S5.1.1. Hoop and longitudinal stress generated by the air expansion (A)

The breaking mechanism discussed here is based on the observation that a rapid temperature increase causes a proportional expansion of the air trapped within the tetrapod cavity. Such an expansion generates an internal pressure acting on the inner surface of the tetrapod tube, as schematically shown in Figure S16a.

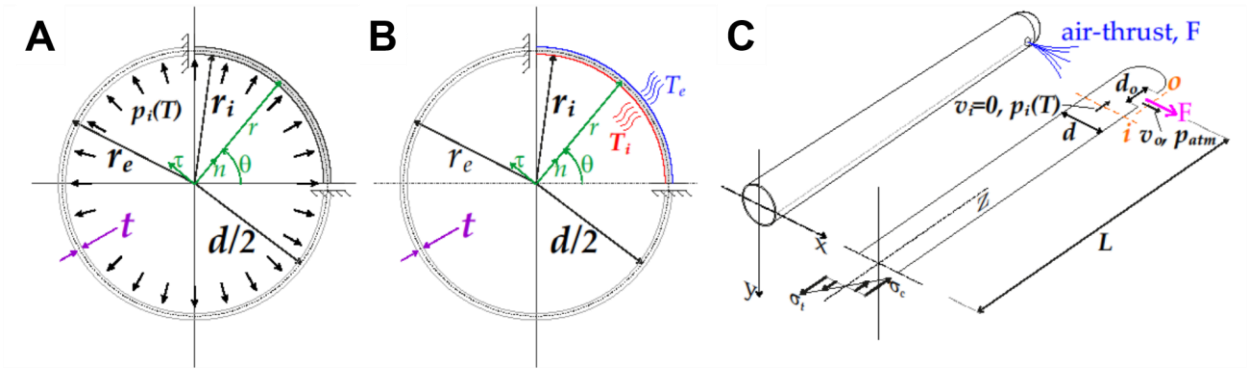

Figure S18. Schematic of the analysed failure mechanisms. (**A**) Hoop and longitudinal stress generated by air expansion, mechanism (A); (**B**) thermoelastic problem of an elastic body subject to a thermal load, mechanism (B); (**C**) longitudinal stress produced by the airflow, mechanism (C).

A real gas that does not act ideally can be described by the generalized Van der Waals equation of state [17]:

$$\left(p + a\frac{n^2}{V^2}\right)(V - nb) = nRT \qquad \text{(S13)}$$

where p is the pressure, a is a coefficient related to the attraction between molecules, n is the number of moles of the gas, V is the volume of the gas, T is the temperature, R is the universal gas constant (R=8.3145 J mol^{-1} K^{-1}), and b is a coefficient dependent on the size of the molecules, respectively.

Since the increase of air pressure due to a heating process is relatively low, it is a good approximation considering the air to be an ideal gas. Under these assumptions, the relation between the state variables is described through the equation of state for an ideal gas (a=b=0):

$$\frac{pV}{T} = nR = const. \qquad \text{(S14)}$$

Assuming the cavity volume of the tetrapod constant during the process (V_i=V_f=V), Equation S2 reduces to the Gay-Lussac's law

$$\frac{p}{T} = const. \qquad \text{(S15)}$$

The previous equation states the direct proportionality between the pressure and the absolute temperature of the gas. By applying Equation S3 at two different states, i.e., an initial state 0 and a final state 1, we can write

$$p_1(T_1) = \frac{p_0}{T_0}T_1 \qquad \text{(S16)}$$

where p_0=p_{atm}=101.325 kPa is the absolute atmospheric pressure, T_0 the initial temperature (293.15 K) and T_1=T_i the final temperature (673.15 K) applied to the sample. The maximum absolute

pressure acting on the cavity is p_1=232.662 kPa. The effective pressure acting on the inner surface of the cavity, p_i(r=r_i), when the temperature T_1 is reached, is

$$p_i = p_1 - p_{atm} = 131.344\ kPa \qquad \text{(S17)}$$

Note the inner pressure p_i, and approximating the actual geometry of the tetrapod tube with an hollow cylinder, it is straightforward to compute the radial and tangential (hoop) stress produced by the internal pressure via the Lamé equations[18]

$$\sigma_r = \frac{r_i^2 p_i}{r_e^2 - r_i^2}\left(1 - \frac{r_e^2}{r^2}\right) \qquad \text{(S18)}$$

$$\sigma_\theta = \frac{r_i^2 p_i}{r_e^2 - r_i^2}\left(1 + \frac{r_e^2}{r^2}\right)$$

Since the cylinder is closed at the ends, a longitudinal stress is also generated

$$\sigma_z = \frac{r_i^2 p_i}{r_e^2 - r_i^2} \qquad \text{(S19)}$$

Considering the actual geometry of the tetrapods, we obtain

$$\sigma_r \cong 0,\ \sigma_{\theta,r_i} = 13.13\ MPa,\ \sigma_{\theta,r_e} = 13.00\ MPa,\ \sigma_z = 6.5\ MPa \qquad \text{(S20)}$$

The estimated tensile stress is in the megapascal range suggesting that this mechanism, most likely, does not lead to the tetrapod failure.

S5.1.2. Thermal stress analysis (B)

In this subsection, the thermoelastic problem of an elastic body subject to a thermal load is discussed and deeply analyzed. In fact, during the experiments, the tetrapods experience a sharp temperature jump of about 380 K in less than 0.4 s. It is well-known that any change in temperature gives rise to stress generation within the material[18–24]; the more abrupt the temperature jump is, the more stress produced is critical, especially for brittle materials which are weak in tension. For the sake of simplicity, we approximated the tetrapod with a long hollow cylinder of inner radius r_i and outer radius r_e, as shown in Figure S16b. We also assumed the temperature field symmetrical about longitudinal axis z. Under these hypotheses, the problem is axially symmetric so that the stress and the temperature fields are a function of only the radial coordinates r (and independent from the tangential and longitudinal coordinates Θ and z, respectively).

In the case of an applied thermal load (and no external forces are present[22]), the stress-strain relations, in cylindrical coordinates, are

$$\varepsilon_r = \frac{1}{E}[\sigma_r - \upsilon(\sigma_\theta + \sigma_z)] + \alpha_T T \qquad \text{(S21)}$$

$$\varepsilon_\theta = \frac{1}{E}[\sigma_\theta - \upsilon(\sigma_r + \sigma_z)] + \alpha_T T$$

$$\frac{1}{E}[\sigma_z - \upsilon(\sigma_\theta + \sigma_r)] + \alpha_T T = 0$$

The equilibrium equation in terms of the radial displacement u_r states

$$\frac{d^2u_r}{dr^2} + \frac{1}{r}\frac{du_r}{dr} - \frac{u}{r^2} = \upsilon^* \frac{dT}{dr},\ \upsilon^* = \frac{1+\nu}{1-\nu} \qquad \text{(S22)}$$

Integrating the previous equation, imposing the traction-free condition on the inner and the outer surface of the cylinder, and assuming the temperature distribution *T(r)*

$$T(r) = T_i + \frac{T_e - T_i}{\ln(r_e/r_i)} \ln\frac{r}{r_i} \qquad \text{(S23)}$$

where T_i and T_e are the inner and outer temperature, respectively, we end up with the closed-form expressions for the stress components as a function of the thermal load T_e-T_i=ΔT, as reported in [22]:

$$\sigma_r = \frac{\alpha_T E}{2(1-\nu)} \frac{\Delta T}{\ln(r_e/r_i)} \left[ln\left(\frac{r_e}{r}\right) + \frac{r_i^2}{r_e^2 - r_i^2}\left(1 - \frac{r_e^2}{r^2}\right) \ln\left(\frac{r_e}{r_i}\right) \right] \qquad \text{(S24)}$$

$$\sigma_\theta = \frac{\alpha_T E}{2(1-\nu)} \frac{\Delta T}{\ln(r_e/r_i)} \left[-1 + ln\left(\frac{r_e}{r}\right) + \frac{r_i^2}{r_e^2 - r_i^2}\left(1 + \frac{r_e^2}{r^2}\right) \ln\left(\frac{r_e}{r_i}\right) \right]$$

$$\sigma_z = \frac{\alpha_T E}{2(1-\nu)} \frac{\Delta T}{\ln(r_e/r_i)} \left[-1 + 2ln\left(\frac{r_e}{r}\right) + \frac{2r_i^2}{r_e^2 - r_i^2} \ln\left(\frac{r_e}{r_i}\right) \right]$$

The tangential and longitudinal stress components attain their maximum numerical values at the inner (r=r_i) and outer (r=r_e) surface of the cylinder; the radial components attain its maximum, approximatively, at the middle of the wall thickness $[r \approx (r_e + r_i)/2 = d/2]$. Considering the actual geometry of the tetrapods, we obtain:

$$\sigma_{r,t,max} = 0.021\ GPa,\ \sigma_{\theta,t,r_e} = 1.246\ GPa,\ \sigma_{z,t} = 1.246\ GPa \qquad \text{(S25)}$$

Therefore, this mechanism, most likely, is the main responsible for breaking the sample, since it is able to generate stresses in the gigapascal range.

S5.1.3. Longitudinal stress produced by the airflow (C)

The breaking mechanism proposed here arises from the observation that upon heating the air expands, leading to an increase of the internal pressure, as already explained in the section 1.1. The air expansion generates an airflow from the cavity to ambient through the voids (generated during the fabrication process) present on the lateral surface of the tetrapod. In the discussion, we consider the critical case of a single void orthogonal to the longitudinal axis and located at the tip of the tetrapod, as shown in Figure S16c. The airflow generates, through the action-reaction

principle, a transverse force acting at the end of the tetrapod. Such a force arises by the accelerating air flowing from a small void. The thrust-pressure relation is obtained exploiting the continuity equation, the momentum equation and the energy equation.

With reference to the control volume defined by the control sections *i* and *o*, the thrust **P** acting at top of the beam can be derived from the momentum equation as

$$\mathbf{P} = \sum \mathbf{F} = \sum_o \beta \dot{m} \mathbf{v} - \sum_i \beta \dot{m} \mathbf{v} \qquad \text{(S26)}$$

where β is a correction factor (for turbulent flows, $\beta \cong 1$ can be assumed), $\dot{m}$ is the mass flow and **v** the velocity.

Assuming $p_0 \cong p_{atm}$, the force *F*, equal to the component of the air thrust **P** along the *x* axis is

$$F \cong \rho_o A_o d_o^2 \quad \text{(S27)}$$

where ρ_o is the air density, d_o the diameter of the void, and A_o is its area. The air, assumed dry, is a compressible fluid whose density depends on pressure and temperature

$$\varrho(p,T) \cong \varrho_{dry}(p,T) = \frac{p}{R_{spec}T} \qquad \text{(S28)}$$

where *T* is the absolute temperature [K], *p* the absolute pressure [Pa], R_{spec}=287.058 J kg^{-1} K^{-1}) the specific gas constant. For adiabatic and isoentropic compression/expansion processes of an ideal gas, the relations among its temperature *T*, pressure *p* and density ϱ are $p^{1-\gamma}T^{\gamma} = const.$, $\varrho/p^{1/\gamma} = const.$, where γ is the heat capacities ratio C_p/C_v, equal to 7/5 for air.

In the case of a steady flow with no shaft work, negligible change in elevation takes place adiabatically, the energy balance (first law of thermodynamics) writes

$$h + \frac{v^2}{2} = \delta s_{irr} \qquad \text{(S29)}$$

where *v* is the speed flow, *h* is the enthalpy of the system and δs_{irr} is the dissipation. The enthalpy can be expressed as a function of the heat capacity ratio, the pressure and the density as

$$dh = c_p dT \Rightarrow h = \frac{\gamma}{\gamma-1}\frac{p}{\varrho} \qquad \text{(S30)}$$

Therefore, the energy balance law between the control sections *i* and *o*, for the ideal case of no-dissipation (δs_{irr}=0), states

$$\frac{\gamma}{\gamma-1}\frac{p_i}{\varrho_i} = \frac{v_o^2}{2} + \frac{\gamma}{\gamma-1}\frac{p_o}{\varrho_o} \quad \text{(S31)}$$

By applying Equations S14 and S18, it is possible to derive the analytical relation between the air thrust *F* and the internal pressure p_{in}

$$F = 2A_o \frac{\gamma}{1-\gamma} \frac{p_i^{(\gamma-1)/\gamma}}{p_{atm}^{-1/\gamma}} \left[\left(\frac{p_i}{p_{atm}} \right)^{(1-\gamma)/\gamma} - 1 \right] \quad \text{(S32)}$$

The maximum force F_{max} acting at the tip is attained when p_i=131.344 kPa, as computed in the subsection 1.1. The maximum tensile stress σ_t produced by the force F, is evaluated considering the tetrapod as a cantilever beam subjected to a concentrated force at its free end:

$$\sigma_{t,max} = \frac{4F_{max}Lr_e}{\pi(r_e^4 - r_i^4)} \cong \frac{4F_{max}L}{\pi t d^2} \quad \text{(S33)}$$

Considering the actual geometry of the tetrapods, the tensile stress is evaluated for three different values of the void diameters (10 nm, 25 nm and 50 nm). For such voids, we obtain the corresponding values

$$\sigma_{t,max} = \{0.012, 0.077, 0.31\} MPa \quad \text{(S34)}$$

The estimated tensile stress is in the megapascal range, suggesting that this mechanism, most likely, does not lead to the tetrapod failure.

S5.2. Finite element simulations

We performed several Abaqus simulations with the purpose to validate the mechanical mechanisms discussed in the subsections 1.1 and 1.2 thoroughly. The material properties implemented in the analysis are those listed in section 1.2. First, the simulations were performed considering the tetrapod arms to be cylindrical, as assumed in the analytical calculations. Such simulations confirm the predicted values, with an error of less than 0.5%. Then, to give a better comparison with the real experiments, we approximated the tetrapods with an axially symmetric truncated hexagonal hollow prism. The geometry was designed in SolidWorks and then imported in Abaqus. Due to the symmetry of the problem, we modelled only one-fourth of the solid, by imposing the symmetric conditions on the vertical and horizontal axes, as shown in Figure S15. We carried out the three different simulations discussed below, all considering the hexagonal geometry. In the analysis, we refined the mesh in the corner area where we observed the stress concentration. In particular, we performed a mesh-refinement study to estimate the optimal mesh size so that the results are mesh-independent.

S5.2.1. Hexagonal hollow prism subject to an internal pressure (A)

We performed an Abaqus/Standard static simulation to estimate the critical stress produced by an increasing pressure (from 0 to $p_{i,max}$=131.344 kPa, see section 1.1) applied on the inner surface of the tetrapod, as shown in Figure S17.

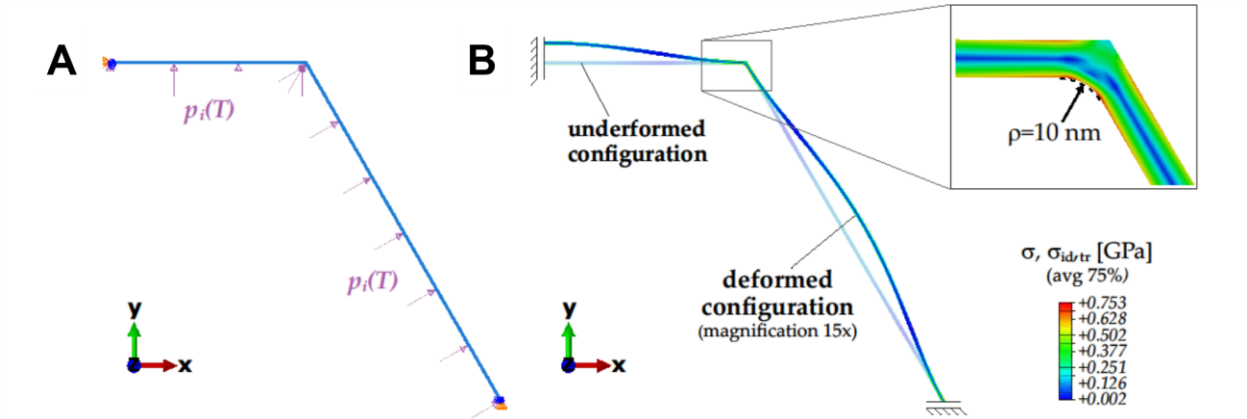

Figure S19. (**A**) Modelling of the quarter of a truncated hexagonal hollow prism (t=10 nm, d=2 µm, ϱ=10 nm) subject to an internal pressure $p_i(T)$. (**B**) The deformed configuration (magnification 15x) is superimposed to the undeformed shape. The inset depicts a detail of the Tresca maximal stress distribution around the corner.

The air expansion, upon heating, produces a pressure proportional to the temperature increase. We discretized the quarter of a truncated hexagonal hollow prism with 7231 2D elements (S8R). The numerical results, for the geometrical parameters t=10 nm, d=2 µm, ϱ=10 nm, provide an ideal Tresca maximal stress of about 753 MPa, higher than those obtained considering a cylindrical geometry.

S5.2.2. Thermo-mechanical analysis of the hexagonal hollow prism subject to the temperature jump (B)

We carried out an Abaqus/coupled temperature-displacement simulation to estimate the critical stress produced by the sharp temperature jump of 380 K. For the geometry reported in Figure S15, we considered a section whose circumferential circle diameter is d=1 µm. We modelled the quarter of a ring with 7231 plane-strain quadratic 2D coupled temperature-displacement elements (CPE8RT), as shown in Figure S18. By performing this analysis, we obtain for the geometrical parameters t=10 nm, d=2 µm, ϱ=10 nm, an ideal Tresca maximal stress of about 2.05 GPa, higher than those obtained considering a cylindrical geometry.

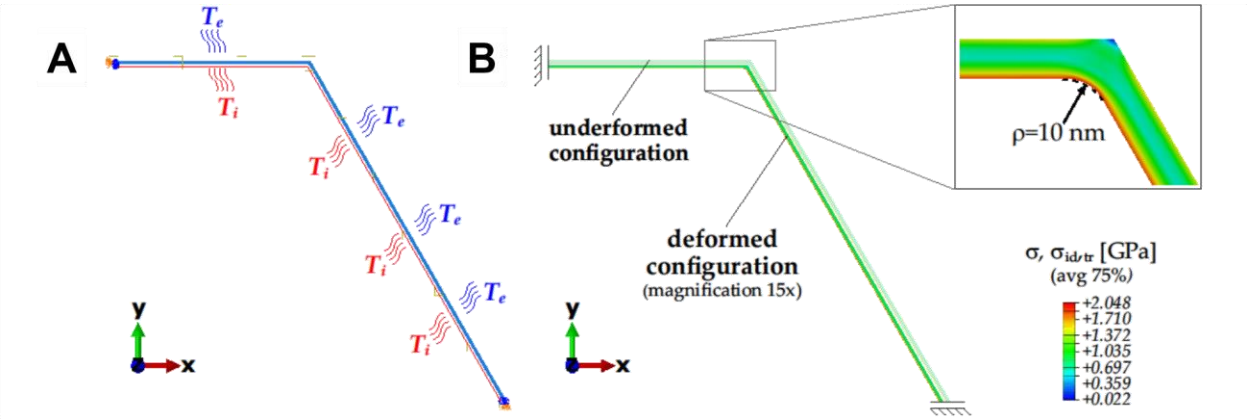

Figure S20. (**A**) Modelling of the thermo-mechanical analysis quarter of a truncated hexagonal hollow prism (t=10 nm, d=2 μm, ϱ=10 nm) subject to a temperature jump $\Delta T = -380\ K$. (**B**) The deformed configuration (magnification 15x) is superimposed to the undeformed shape. The inset depicts a detail of the Tresca maximal stress distribution around the corner.

S5.2.3 Thermo-mechanical analysis of the hexagonal hollow prism subject to the temperature jump and the internal pressure (AB)

We combined the previous two simulations in order to mimic, as much as possible, the real experiment by applying simultaneously the temperature jump and the internal pressure (Figure S19). In the analysis, we assumed the model of the above thermo-mechanical analysis. By performing this analysis, we obtained, for the geometrical parameters t=10 nm, d=2 μm, ϱ=10 nm, an ideal Tresca maximal stress of about 2.4 GPa. Accordingly, we estimate the tetrapod strength is less than 2.4 GPa.

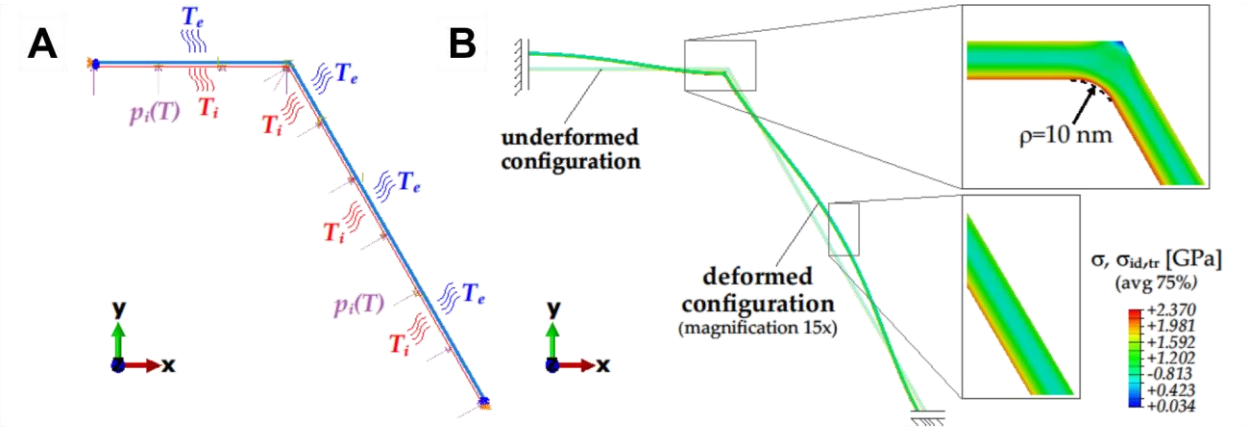

Figure S21. (**A**) Modelling of the quarter of a truncated hexagonal hollow prism (t=10 nm, d=2 μm, ϱ=10 nm) subject to a simultaneous temperature jump $\Delta T = -380\ K$ and an internal pressure $p_i(T)$. (**B**) The deformed configuration (magnification 15x) is superimposed to the undeformed shape. The inset depicts a detail of the Tresca maximal stress distribution around the corner and in the middle of one side.

S5.3 Parametric analysis

This section is devoted to estimating how the Tresca maximal stress $\sigma_{id,tr}$ varies for each combination of the geometrical input parameters, namely the average wall thickness *t*, the tube diameter *d* and also the junction (inner) fillet radius ϱ. The analysis was conducted approximating the tetrapod shape with a truncated hexagonal hollow prism. For this purpose, we developed a specific Python script that programmatically generates the geometries and runs the 54 simulations. The outcomes obtained from Abaqus simulations are summarized for the failure mechanisms (A), (B) and (AB) in Tables S2, S3, and S4, respectively. The analysis was carried out by varying the average wall-thickness *t*={10, 20, 30} nm, the tube diameter *d*={1, 2, 3} µm and the junction (inner) fillet radius ϱ ={2, 10} nm. The results are discussed in the next paragraphs for the failure mechanisms (A), (B) and (AB).

S5.3.1. Mechanism (A)

The results reported in Table S2 show that the Tresca maximal stress $\sigma_{id,tr}$ increases with increasing tube diameter *d* and decreases with increasing wall thickness *t*, similarly to what is predicted by Equation S6 (for the tangential stress σ_t). Moreover, the Tresca stress is highly dependent on the fillet (inner) radius ϱ at the corners. As aspected, the lower the fillet radius is, the higher is the Tresca maximal stress $\sigma_{id,tr}$.

Table S2. Failure mechanisms (A): Tresca maximal stress $\sigma_{id,tr}$.obtained from the Abaqus simulations for each combination of the input geometrical parameters; wall thickness *t*={10, 20, 30} nm, a tube diameter *d*={1, 2, 3} µm and a junction (inner) fillet radius ϱ ={2, 10} nm.

Mech. (A)	*d*=1 µm		*d*=2 µm		*d*=3 µm	
$\sigma_{id,tr}$. [MPa]	ϱ=2 nm	ϱ=10 nm	ϱ=2 nm	ϱ=10 nm	ϱ=2 nm	ϱ=10 nm
t=10 nm	275.2	185.2	1093	753.0	2467	1704
t=20 nm	90.64	59.18	359.5	235.1	807.7	527.9
t=30 nm	47.02	31.13	184.14	122.8	413.2	275.3

S5.3.2. Mechanism (B)

The results reported in Table S3 show that Tresca maximal stress $\sigma_{id,tr}$ is almost independent of the tube diameter *d* and increases with increasing wall thickness *t*, similar to what was predicted by Equation S11 (for the tangential stress σ_t). Moreover, the Tresca stress depends, as for the mechanism (A), on the fillet (inner) radius ϱ at the corners. As expected, the lower the fillet radius is, the higher is the Tresca maximal stress $\sigma_{id,tr}$.

Table S3. Failure mechanisms (B)

Mech. (B)	d=1 μm		d=2 μm		d=3 μm	
$\sigma_{id,tr}$. [MPa]	ϱ=2 nm	ϱ=10 nm	ϱ=2 nm	ϱ=10 nm	ϱ=2 nm	ϱ=10 nm
t=10 nm	2290	2048	2287	2048	2291	2048
t=20 nm	2695	2184	2700	2184	2704	2184
t=30 nm	3107	2310	3099	2311	3102	2312

S5.3.3. Mechanism (AB)

For this coupled mechanism, i.e., a combination of the mechanisms (A) and (B), the parametric analysis shows that the Tresca maximal stress $\sigma_{id,tr}$.increases with increasing tube diameter d and decreasing fillet radius ϱ. Analyzing the results reported in Table S2, we observe that there is not a clear relation between the Tresca stress and the wall thickness t. For instance, for a tube diameter d=1 μm, an increase of the wall thickness always leads to an increase of the Tresca maximal stress $\sigma_{id,tr}$. On the contrary, for the tube diameters d=2 μm and d=3 μm, we observe that the Tresca stress decreases moving from t=10 nm to t=20 nm and then increases moving from t=20 nm to t=30 nm. This peculiar behavior can be explained by carefully observing the Tresca stress/wall-thickness relation for the mechanisms (A) and (B). In fact, for d=1 μm, the mechanism (B) is dominant over the mechanism (A) and, therefore, an increase in the wall thickness leads to an increase in the Tresca stress. For d=2 μm and d=3 μm, the mechanisms (A) and (B) play a similar role; therefore, an optimal wall thickness could emerge.

Table S4. Failure mechanisms (AB)

Mech. (AB)	d=1 μm		d=2 μm		d=3 μm	
$\sigma_{id,tr}$. [MPa]	ϱ=2 nm	ϱ=10 nm	ϱ=2 nm	ϱ=10 nm	ϱ=2 nm	ϱ=10 nm
t=10 nm	2405	2127	3157	2370	4539	3156
t=20 nm	2786	2209	3059	2285	3512	2411
t=30 nm	3154	2323	3283	2364	3515	2430

S6. Pump Efficiency Calculation

Considering the experimental setup for the air flow measurement presented in Figure 2A and B in an ideal case, the generated expansion of the air contained inside the F-AM (volume of ~0.16 ml) can be calculated assuming ideal gas behavior and isobaric conditions as follows

$$V_2 = V_1 \frac{T_2}{T_1} \qquad \text{(S35)}$$

where T_1 and T_2 correspond to the starting and maximum temperatures, respectively, and V_1 and V_2 are the air volumes before and after expansion. Inserting V_1=0.16 ml, T_1=293.15 K, and T_2=673.15 K into Equation S35, the expanded air volume is V_2=0.367 ml. Hence, the total air flow is given by

$$\Delta V = V_2 - V_1 = 0.207\ ml \qquad \text{(S36)}$$

However, the measured value of the total air flow approaches a maximum value of about 0.085 ml at 100 ms PPW (Figure 4D). The efficiency of the pump can then be calculated as

$$\eta = \frac{0.085\ ml}{0.207\ ml} * 100\% = 41\% \qquad \text{(S37)}$$

The efficiency of the EPRAE-based micro-pump could be further increased by decreasing the size of the metal contacts, which act as heat sinks and reduce the Joule-heating efficiency of the F-AM close to the contact surface. Nevertheless, in view of the unoptimized experimental setup, the achieved efficiency of 41% is already considerably high.

Gas Flow and Pressure

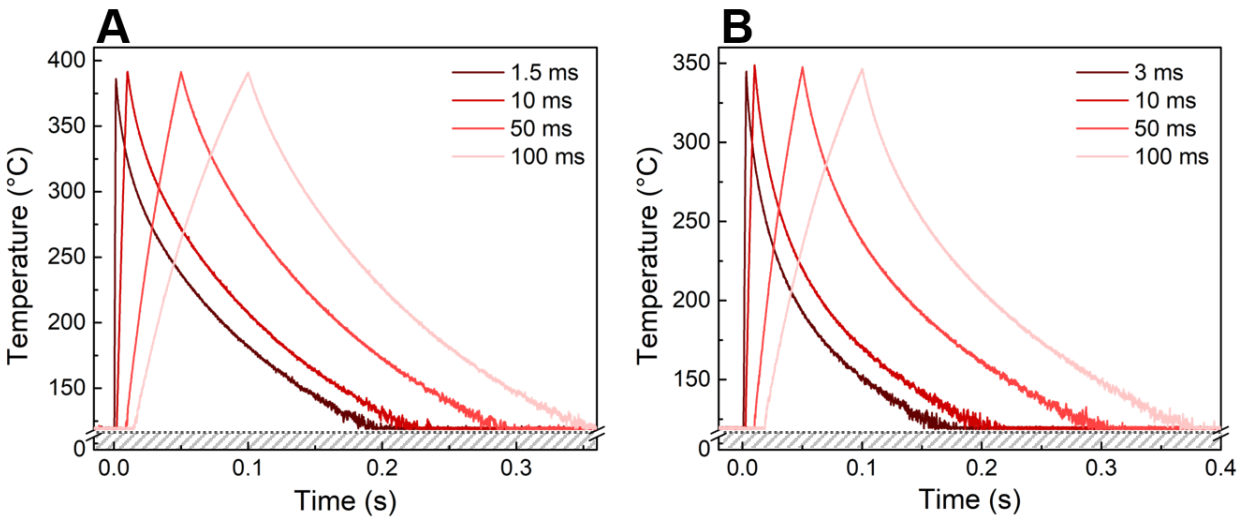

Figure S22. Temperature-time profiles of Aero-EG for (**A**) the corresponding gas flow measurements with different pulse lengths (Figure 4C, main manuscript) and (**B**) the corresponding pressure measurements with different pulse lengths (Figure 4G, main manuscript).

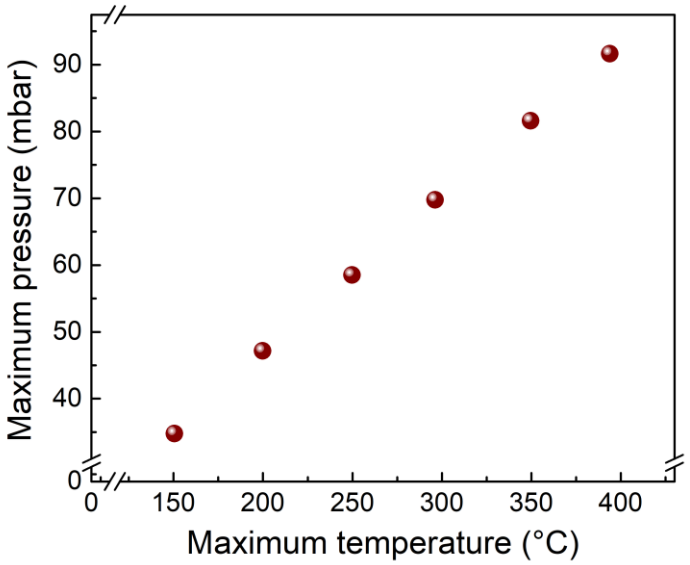

Figure S23. Pressure-temperature profile of Aero-EG for EPRAE pulses (pulse length 50 ms) with increasing power in an isochoric system, resulting in a linear pressure-temperature relation.

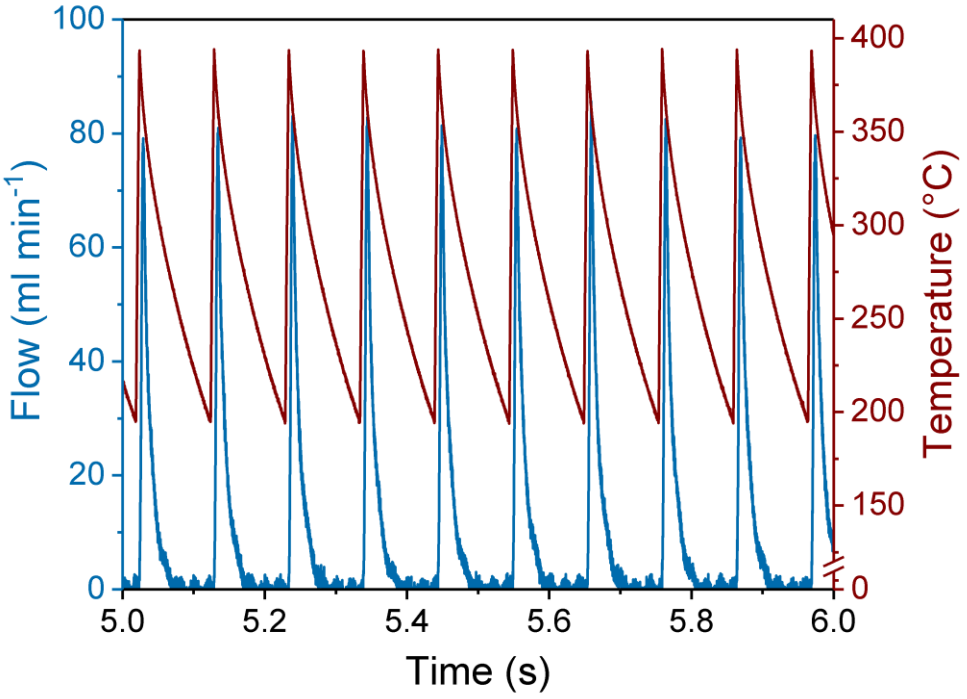

Figure S24. Temperature-time profile and corresponding gas flow resulting from rapid cyclic Joule heating of Aero-EG with 5 ms power pulse width, a power pulse frequency of 9.5 Hz.

Micro-Thruster

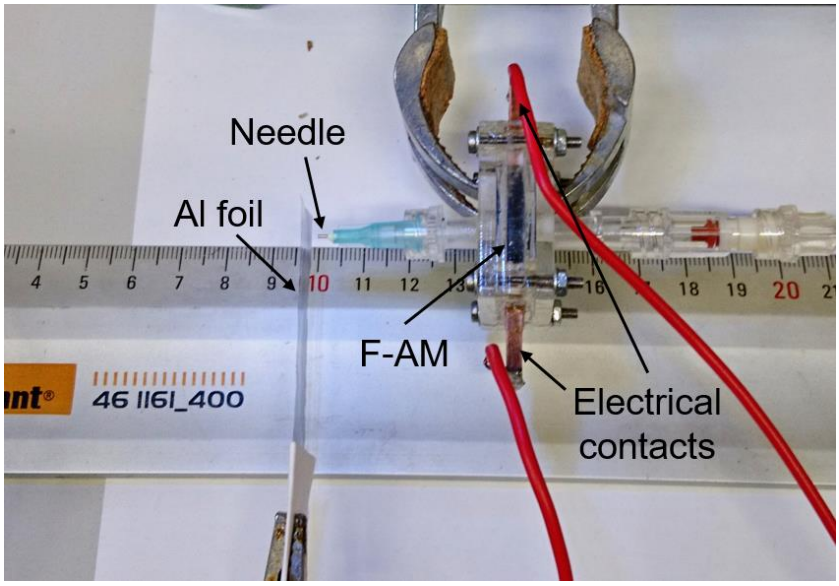

Figure S25. Photograph of employed setup for the creation of rapid cyclic air thrusts for the movement of the Al foil.

Thermo-Mechanical Micro-Actuator

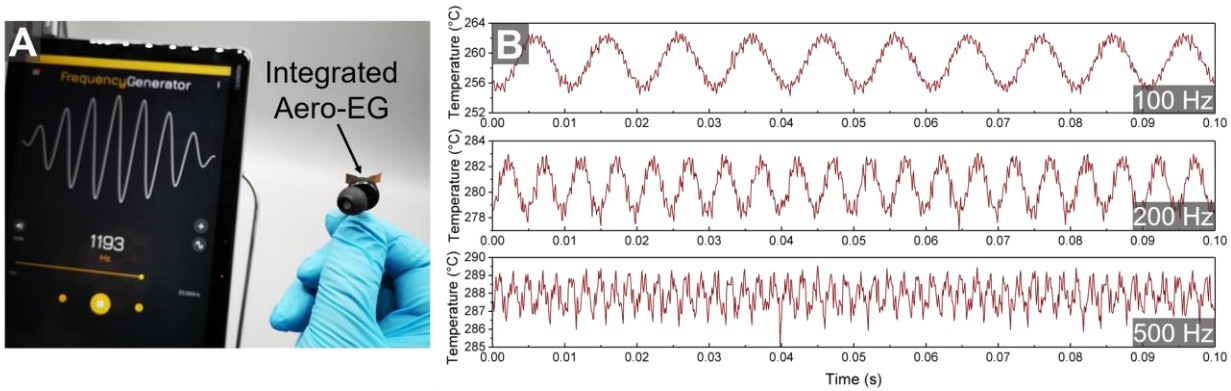

Figure S26. Freestanding, omnidirectional thermophones. (**A**) Photograph of a F-AM-based in-ear thermoacoustic loudspeaker connected to a tablet. By applying different frequencies (using a frequency generator app), sound is emitted. (**B**) Temperature-time profiles for Joule-heating and cooling cycles of a F-AM for different applied frequencies.

Gas Flowmeter

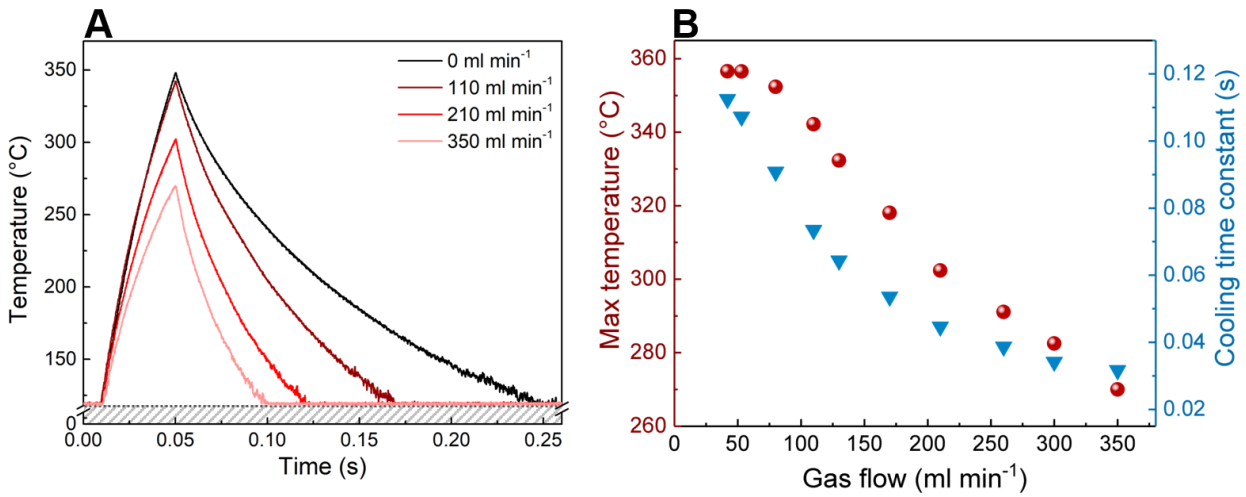

Figure S27. Exploitation of EPRAE for gas flowmeter. (A) Temperature-time profiles of Aero-EG during EPRAEs with a peak power of ~9 W and a power pulse width of 50 ms for different air flows. (**B**) The resulting change of maximum temperature and cooling time constants is plotted versus the used gas flow.

Supplementary Movies

Movie S1.

Concept of electrically powered repeatable air explosions (EPRAE), demonstrated by applying cyclic power pulses to Aero-EG to heat the F-AM to 400 °C within 1.7 ms. The resulting explosion-like gas expansion out of the F-AM is indicated by the clicking sound and visualized by the smoke which becomes displaced by the expanded gas.

Movie S2.

Application of ultra-fast (50 µs) and high-power (576 W) Joule-heating pulse to Aero-EG, resulting in extremely fast heating ($>4\times10^6$ K s^{-1}) of the contained air and, consequently, partial bursting of macroscopic parts of the sample.

Movie S3.

Demonstration of EPRAE for several applications, including a micro-pump, micro-thruster, micro-actuator, and a thermophone.

Movie S4.

Demonstration of weight-lifting using a F-AM based electro-pneumatic actuator, actuating more than the 10^6-fold of its own weight. To increase the temperature difference during Joule heating of the F-AM and, thus, the volume expansion, the experiment is conducted in inert nitrogen atmosphere.

Movie S5.

Demonstration of high sensitivity of a F-AM to small air flows during constant Joule heating with constant power.

References

1. Shaygan Nia, A. *et al.* Carbon-Supported Copper Nanomaterials. Recyclable Catalysts for Huisgen 3+2 Cycloaddition Reactions. *Chemistry (Weinheim an der Bergstrasse, Germany)* **21,** 10763–10770; 10.1002/chem.201501217 (2015).
2. Shaygan Nia, A. *et al.* Click chemistry promoted by graphene supported copper nanomaterials. *Chemical communications (Cambridge, England)* **50,** 15374–15377; 10.1039/C4CC07774A (2014).
3. Mishra, Y. K. *et al.* Fabrication of Macroscopically Flexible and Highly Porous 3D Semiconductor Networks from Interpenetrating Nanostructures by a Simple Flame Transport Approach. *Part. Part. Syst. Charact.* **30,** 775–783; 10.1002/ppsc.201300197 (2013).
4. Mishra, Y. K. *et al.* Direct Growth of Freestanding ZnO Tetrapod Networks for Multifunctional Applications in Photocatalysis, UV Photodetection, and Gas Sensing. *ACS applied materials & interfaces* **7,** 14303–14316; 10.1021/acsami.5b02816 (2015).
5. Rasch, F. *et al.* Wet-Chemical Assembly of 2D Nanomaterials into Lightweight, Microtube-Shaped, and Macroscopic 3D Networks. *ACS applied materials & interfaces* **11,** 44652–44663; 10.1021/acsami.9b16565 (2019).
6. Chen, Z. *et al.* Three-dimensional flexible and conductive interconnected graphene networks grown by chemical vapour deposition. *Nature materials* **10,** 424–428; 10.1038/nmat3001 (2011).
7. Menzel, R. *et al.* Joule Heating Characteristics of Emulsion-Templated Graphene Aerogels. *Adv. Funct. Mater.* **25,** 28–35; 10.1002/adfm.201401807 (2015).
8. Andrea C. Ferrari & Denis M. Basko. Raman spectroscopy as a versatile tool for studying the properties of graphene. *Nature Nanotech* **8,** 235–246; 10.1038/nnano.2013.46 (2013).
9. Couzi, M., Bruneel, J.-L., Talaga, D. & Bokobza, L. A multi wavelength Raman scattering study of defective graphitic carbon materials. The first order Raman spectra revisited. *Carbon* **107,** 388–394; 10.1016/j.carbon.2016.06.017 (2016).
10. Eckmann, A. *et al.* Probing the Nature of Defects in Graphene by Raman Spectroscopy. *Nano letters* **12,** 3925–3930; 10.1021/nl300901a (2012).
11. Ferrari, A. C. & Robertson, J. Interpretation of Raman spectra of disordered and amorphous carbon. *Phys. Rev. B* **61,** 14095–14107; 10.1103/PhysRevB.61.14095 (2000).
12. Parvez, K. *et al.* Exfoliation of graphite into graphene in aqueous solutions of inorganic salts. *Journal of the American Chemical Society* **136,** 6083–6091; 10.1021/ja5017156 (2014).
13. Politano, A. & Chiarello, G. Probing the Young's modulus and Poisson's ratio in graphene/metal interfaces and graphite. A comparative study. *Nano Res.* **8,** 1847–1856; 10.1007/s12274-014-0691-9 (2015).
14. Shaina, P. R., George, L., Yadav, V. & Jaiswal, M. Estimating the thermal expansion coefficient of graphene. The role of graphene-substrate interactions. *Journal of physics. Condensed matter : an Institute of Physics journal* **28,** 85301; 10.1088/0953-8984/28/8/085301 (2016).
15. Fugallo, G. *et al.* Thermal conductivity of graphene and graphite. Collective excitations and mean free paths. *Nano letters* **14,** 6109–6114; 10.1021/nl502059f (2014).
16. Li, Q.-Y. *et al.* Measurement of specific heat and thermal conductivity of supported and suspended graphene by a comprehensive Raman optothermal method. *Nanoscale* **9,** 10784–10793; 10.1039/C7NR01695F (2017).
17. Çengel, Y. A. & Cimbala, J. M. *Fluid mechanics. Fundamentals and applications.* 3rd ed. (McGraw-Hill, New York, NY, 2014).

18. Timošenko, S. P. & Goodier, J. N. *Theory of elasticity.* 3rd ed. (McGraw-Hill, Auckland, 2004).
19. Boley, B. A. On thermal stresses and deflections in thin rings. *International Journal of Mechanical Sciences* **11,** 781–789; 10.1016/0020-7403(69)90025-3 (1969).
20. Boley, B. A. & BARREKETTE, E. S. Thermal Stress in Curved Beams. *Journal of the Aerospace Sciences* **25,** 627–630; 10.2514/8.7814 (1958).
21. C. A. Sciammarella & D. Sturgeon. Thermal stresses at high temperatures in stainless-steel rings by the moiré method. *Experimental Mechanics* **6,** 235–243; 10.1007/BF02327306 (1966).
22. Eslami, M. R. *et al. Theory of elasticity and thermal stresses. Explanations, problems and solutions / M. Reza Eslami, Richard B. Hetnarski, Józef Ignaczak, Naotake Noda, Naobumi Sumi, Yoshinobu Tanigawa* (Springer, Dordrecht, 2013).
23. Fettahlioglu, O. A. & Steele, T. K. THERMAL DEFORMATIONS AND STRESSES IN CIRCULARLY CURVED THIN BEAMS AND RINGS. *Journal of Thermal Stresses* **11,** 233–255; 10.1080/01495738808961934 (1988).
24. Forray, M. Thermal Stresses in Rings. *Journal of the Aerospace Sciences* **26,** 310–311; 10.2514/8.8053 (1959).